Doctoral Dissertation (Censored)

博士論文（要約）

Bis(diimino)metal Complex-based Coordination Nanosheets towards Energy Storage Applications

（ビス（ジイミノ）金属錯体を骨格とした配位ナノシートのエネルギー貯蔵への応用）

A Dissertation Submitted for the Degree of Doctor of Philosophy
December 2019

令和元年 12 月博士（理学）申請

Department of Chemistry, Graduate School of Science,

The University of Tokyo

東京大学大学院理学系研究科

化学専攻

Keisuke Wada

和田　慶祐

Abstract

In my Ph.D. thesis, the electrochemical and related properties of bis(diimino)metal coordination nanosheets were studied, aiming at energy storage applications using those nanosheets as electrode materials.

In chapter 1, the importance of metal organic frameworks and their applications including electrochemical energy storages are described. As a state of the art class of MOFs, electronically conductive coordination nanosheets are also introduced.

In chapter 2, synthesis, characterization and electrochemistry-related properties of bis(diimino)nickel coordination nanosheets are described. Electrochemical measurements of the material revealed its promising energy storage function based on unique multielectron transfer reactions. Mechanisms of the electrochemical behavior were further studied using experimental and theoretical techniques.

In chapter 3, bis(diimino)cobalt coordination nanosheet and bis(diimino)copper coordination nanosheet were synthesized, and their electrochemical properties associated with the metal species were investigated. While the former material was redox-inactive, the latter exhibited significantly high capacity owing to metal-ligand cooperating redox reactions.

In chapter 4, I have developed heterometal bis(diimino)cobalt-nickel coordination nanosheets, and effects of the heterometal structures on their electrochemical properties were studied. Increasing the content amount of Ni, the material was gradually redox-activated and showed enhanced energy storage functions at the specific condition.

Finally in chapter 5, the conclusions throughout this work were described.

Table of Contents

Chapter 1

Introduction

1.1 Metal organic frameworks

Among various types of metal-containing materials, metal organic frameworks, (MOFs), or sometimes referred to as porous coordination polymers, are exceptional in degree of tunability on their structure designs and resulting diverse physical/chemical properties.[1] MOFs are the materials built from metal cations as "nodes" and organic ligands as "linkers", which form structures with crystalline ordering. Owing to the almost unlimited combination numbers of the "nodes" and "linkers", numerous types of MOFs have been synthesized and their properties were investigated, aiming at emergence of targeted properties for practical applications[1c-d,2] (Figure 1.1.1).

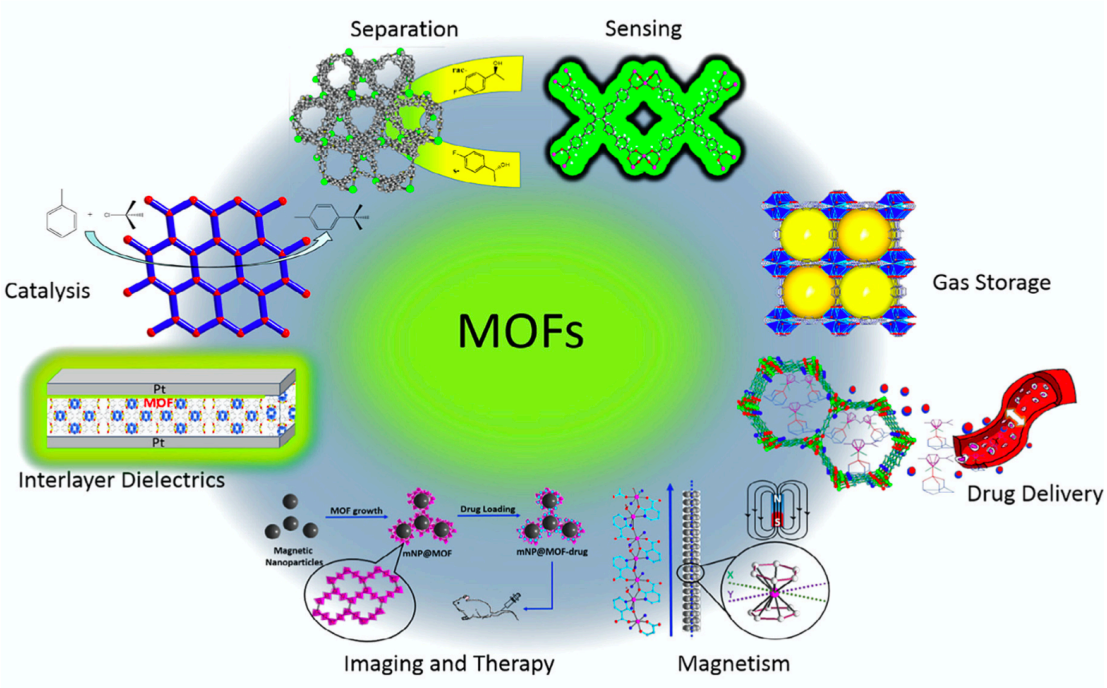

Figure 1.1.1. Numberless types of MOFs with respective functionalities have been developed towards diverse applications. Adapted with permission from reference 2a. Copyright © 2018 Elsevier B.V. All rights reserved.

Upon development of MOFs, one of the major interests for researchers is precisely defined shapes and sizes of porous cavities, which allows us to obtain large surface area and other functionalities.[1a] The early compounds in a class of MOFs were synthesized in the last century using relatively small organic linkers such as nitrile or bipyridine

to form extended crystal structures.[3] However, in those studies, permanent porosity of the compounds were not well demonstrated. The first study proving the permanent porosity was reported with the layered zinc terephthalate MOF,[4] being followed by the pioneering study of MOF-5 which had stable and highly porous structures, achieving Brunauer-Emmett-Teller (BET) surface area of 2320 cm^2/g (Figure 1.1.2).[5] Rationally designed topology and sizes of pores by changing metal cations and organic linkers provided further increase of BET surface area[6] that is higher than 7000 cm^2/g for some compounds.[6b]

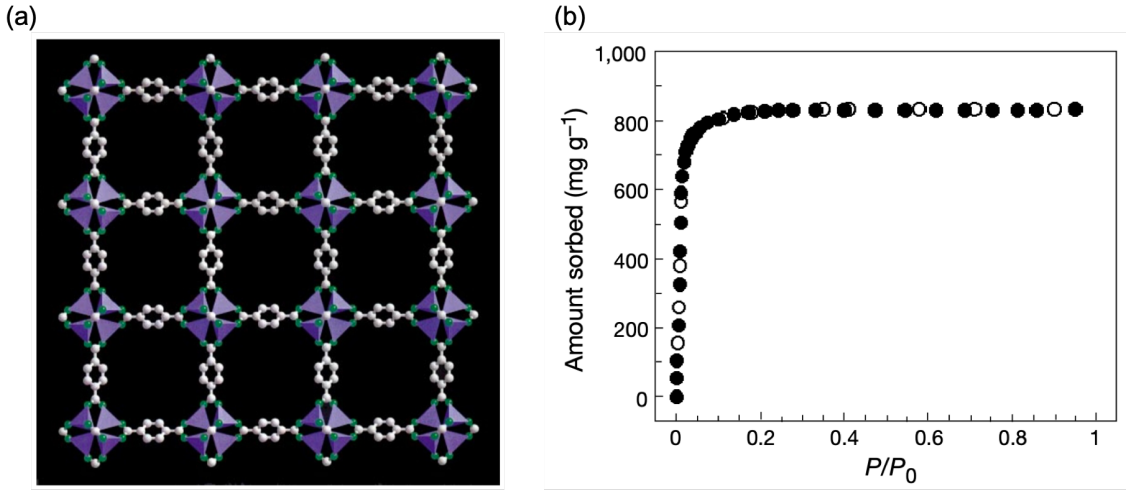

Figure 1.1.2. (a) Simplified structure of MOF-5 framework shown along the a-axis (C; gray and O; green) and (b) nitrogen gas sorption isotherm of MOF-5 at 78 K. (c) BET surface areas of MOFs and typical porous materials determined by gas sorption measurements. Adapted with permission from reference 5. Copyright © 1999, Springer Nature.

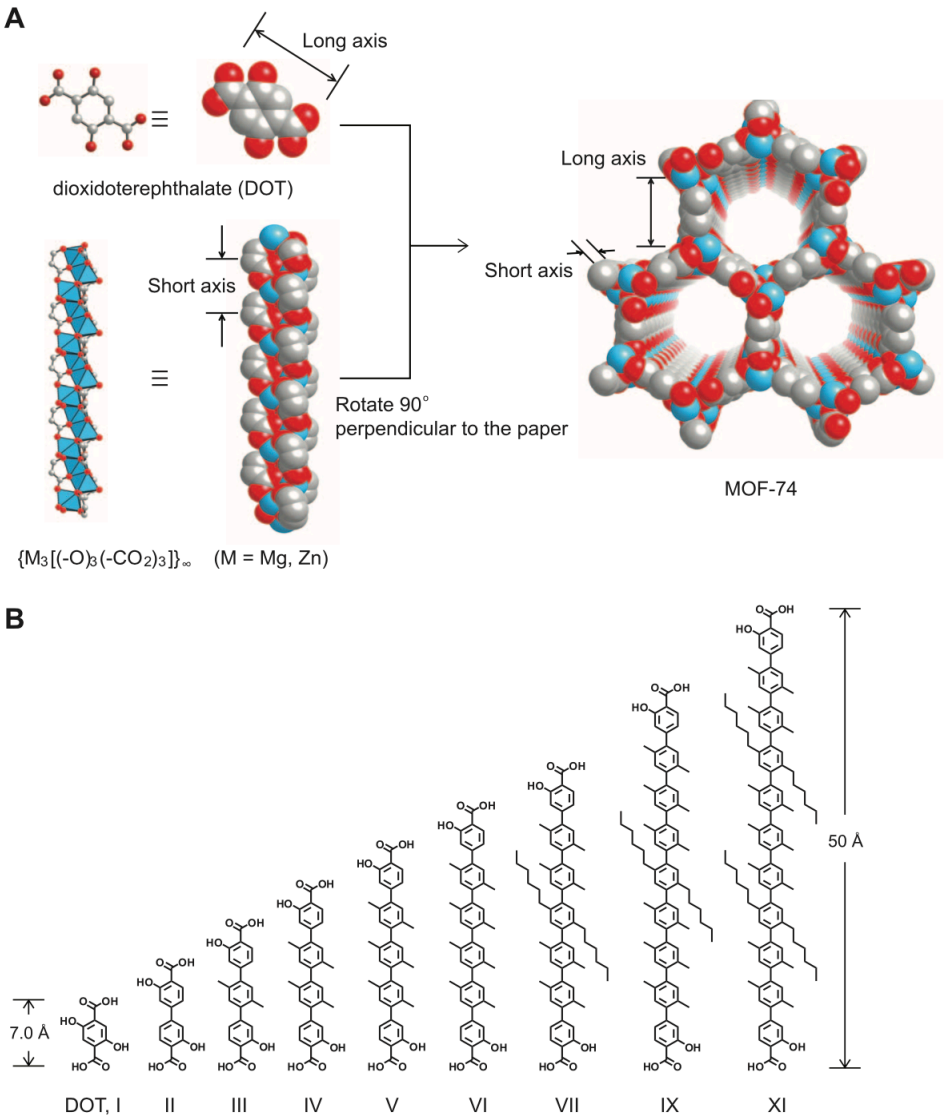

Figure 1.1.3. (A) Crystal structure of MOF-74 (C; gray, O; red, Mg or Zn; blue). H atoms are omitted for clarity. (B) Chemical structures of the organic linkers used for synthesis of MOFs with extended pore apertures. Adapted with permission from reference 7a. Copyright © 2012, American Association for the Advancement of Science.

Besides increase of surface area, synthesis of MOFs possessing large pore volume was intensively tried for the purpose of accommodation of large molecules including proteins, leading to extended applications of MOFs.[7] In order to achieve creation of such large pores, one of the most effective way is to introduce secondary building units (SBUs) having infinitely long rod-shape, which are connected by linkers along perpendicular dimension of those rods.[7b] As an example employing this strategy, MOF-74 was synthesized

from the Mg-contained SBU rod and several types of phenylene-based linkers.[7a] The pore aperture was depending on length of the linkers, and the largest pore (9.8 nm) was obtained with the linker having 11 phenylene units (Figure 1.1.3). This exceptionally large pore aperture was confirmed by electron microscopic techniques, and it was certainly beneficial for accommodation of proteins.

In addition to precisely controlled cavity sizes and surface areas, metal cation sites in frameworks sometimes show chemical interactions with guest molecules.[2b,8] These characteristics allows us to apply MOFs for gas separations by principles of either molecular size or chemical interaction-based sieves.[9] As a representative example using the latter principle, Long *et al.* reported hydrocarbon separation at 318 K with $Fe_2(dobdc)$ ($dobdc^{4-}$ = 2,5-dioxido-1,4-benzenedicarboxylate).[9a] In this work, open Fe(II) coordination sites were found to interact with several hydrocarbon molecules in respectively different strength, being demonstrated by experimental and theoretical methods (Figure 1.1.4). The other type of Fe-based MOFs, $Fe_2(BDP)_3$ (BDP^{2-} = 1,4-benzenedipyrazolate), was also found to be applicable to hexane isomers separation, being reported by the same authors.[9b] The mechanism of the isomers separation was confirmed by Configurational-bias Monte Carlo simulations, which revealed that the separation ability was originated from interactions between the hexane molecules and walls of the framework, rather than metal sites.

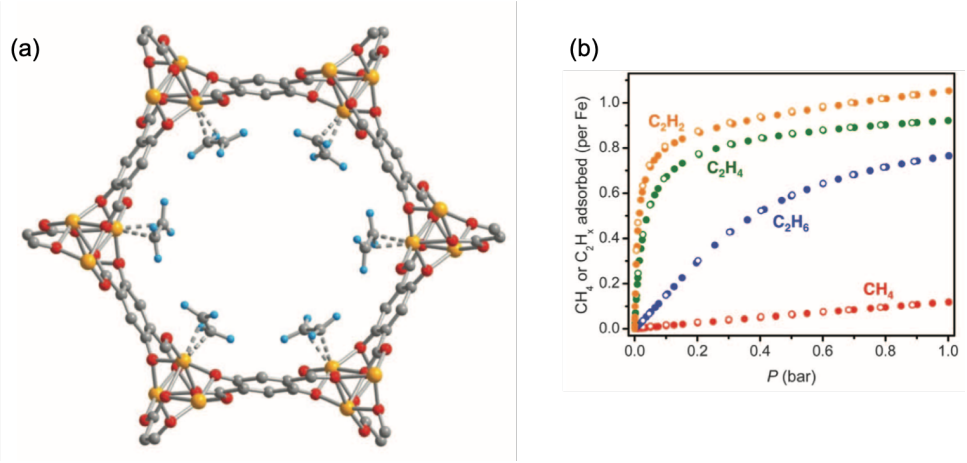

Figure 1.1.4. (a) Chemical structure of $Fe_2(dobdc)$•$2C_2D_4$ (C; gray, O; red, Fe; orange, and D; blue). (b) Hydrocarbon sorption isotherms of $Fe_2(dobdc)$. Adapted with permission from reference 9a. Copyright © 2012, American Association for the Advancement of Science.

Another accessible application of MOFs is catalysis,[1c,10] as the other notable porous inorganic materials such as zeolites.[11] By taking advantages of well-defined reaction spaces in cavities and plenty of active sites including metal nodes, to date, the enormous number of challenges have been done on catalysis with MOFs. The earliest study of the catalysis was reported by Fujita *et al.* in 1994, in which cyanosilylation of aldehydes was catalyzed by Cd(II) ions in $Cd(4,4'\text{-bpy})_2(NO_3)_2$ (Scheme 1.1.1).[10a] In this reaction, they observed selectivity on sizes and shapes of the substrates, and thus the reaction in the framework was confirmed. $[Cu_3(btc)_2(H_2O)_3]$, also known as HKUST-1,[12] is another type of representative MOFs showing catalytic activity on its metal nodes. Kaskel et al. first demonstrated that HKUST-1 could catalyze the cyanosilylation of benzaldehyde or acetone,[10b] being followed by the study of catalytic reactions by anhydrous HKUST-1 that was reported by Alaerts *et al*. Through those studies, the authors confirmed the function of the material as a Lewis acid catalyst.

Scheme 1.1.1. Cyanosilylation of benzaldehyde with a MOF as a heterogenous catalyst.

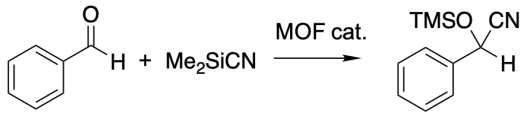

1.2 Metal organic frameworks for energy storage applications

Redox-active MOFs are of great interest for researchers in fundamental science as well as in practical application fields.[13] The origin of the redox reactions of such MOFs is often oxidation state transitions of metal nodes, the reaction principle of which is similar to redox-active inorganic compounds exemplified by metal oxides,[14] metal hydroxides[14b,15] or metal polyanion compounds.[16] Needless to mention, those inorganic compounds are practically used classes in electrochemical energy storage applications including batteries and supercapacitors,[14,15,16] and thus redox-active MOFs would also be candidates for energy storage materials (Figure 1.2.1).[17] Additionally, the MOFs have other two advantages for the application: porosity of the frameworks offers diffusion path for electrolytes, and more importantly, their countlessly varying structures enable us to tailor their electrochemical properties.

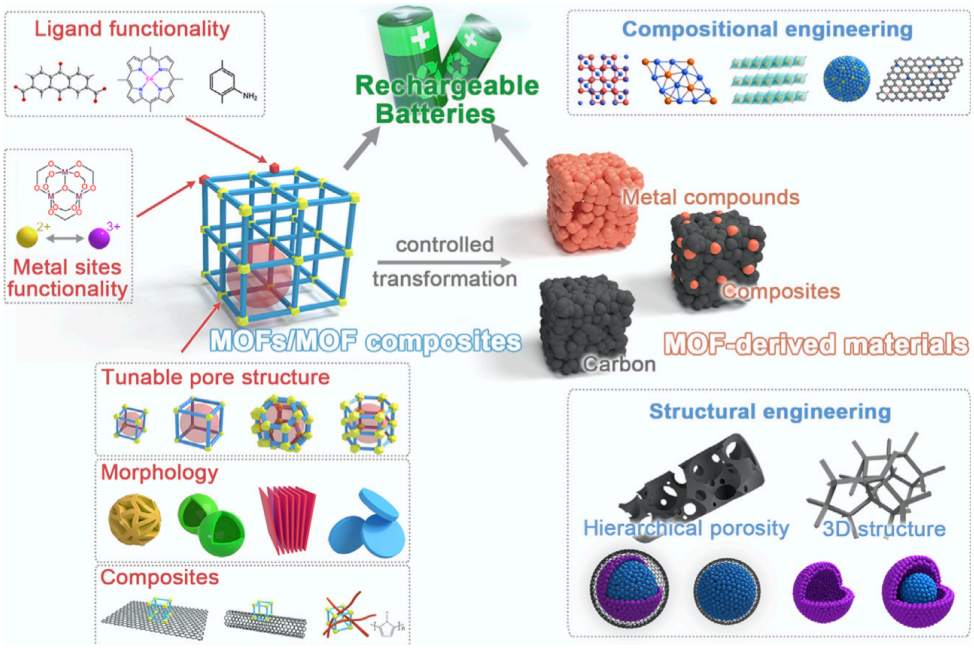

Figure 1.2.1. MOFs, MOF composites and MOF-derived materials for energy storage applications. Adapted with permission from reference 17. Copyright © 2018 Elsevier Inc.

Challenges of employing MOFs in energy storage systems are not limited to an electroactive material in a specific battery. Utilization of MOFs in lithium ion batteries is

the greatest interest for researchers because of their significant importance in the current society.[18] As energy storage systems in the next generation, sodium ion batteries,[19] lithium sulfur batteries[20] or lithium air batteries[21] with MOFs have also attracted attentions. In those cases, rolls of MOFs are varying from electroactive materials[18,19] to ion conductors as solid electrolyte[22] and host materials of other redox species.[20,21] In this thesis, MOF-based electrodes in lithium ion batteries, the most advanced this field are highlighted in the following.

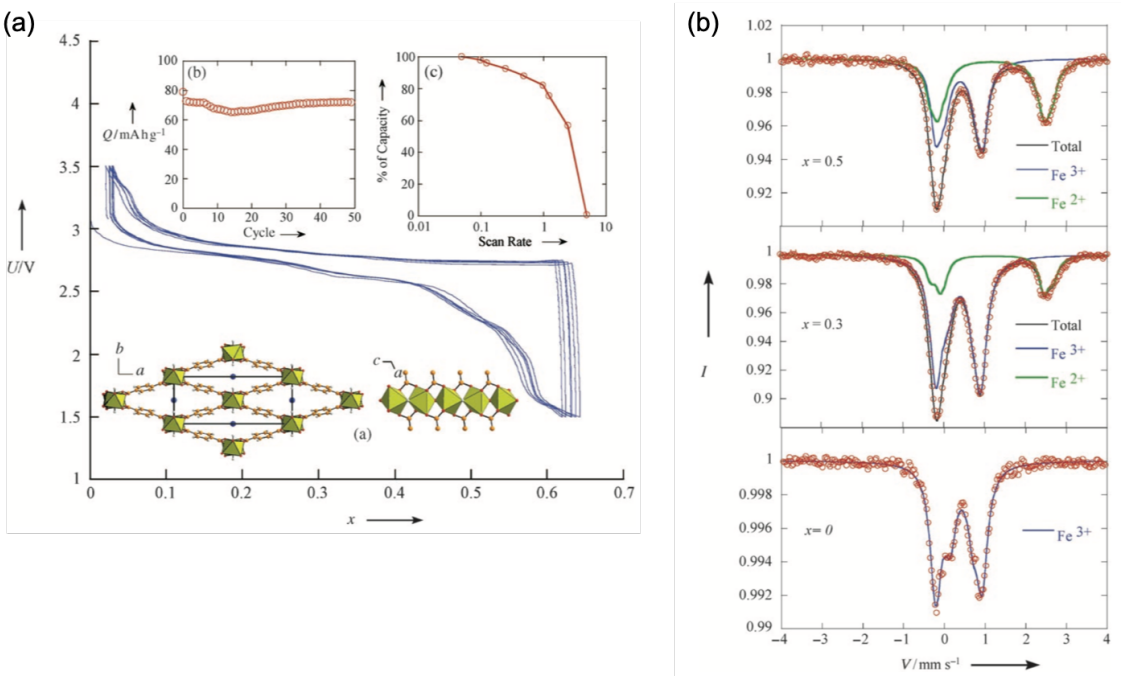

Figure 1.2.2. (a) Charge-discharge profile and (b) ^{57}Fe Mössbauer spectra at 77 K of MIL-53. Adapted with permission from reference 18b. Copyright © 2007 WILEY‐VCH Verlag GmbH & Co. KGaA, Weinheim.

Since the pioneering works of MOF-177 by Li *et al.*[18a] and of MIL-53 by Férey *et al.*[18b], redox-active MOFs have been extensively studied as electrode materials in lithium ion batteries. The former work demonstrated energy storage performance of MOF-177 as an anode material, but irreversibility upon cycling was significantly large and they concluded that MOF-177 was not suitable for an anode.[18a] On the other hand, MIL-53 was employed as a cathode material, and it showed relatively stable cycling but with

moderate specific capacity (75 mAh/g, or 0.6 Li atoms per formula unit).[18b] In addition to a voltage profile during cycles, further detailed investigation revealed that the origin of the energy storage function was redox couple of Fe^{2+}/Fe^{3+}, being accompanied by the crystal phase transitions (Figure 1.2.2).

As the above work of MIL-53, MOF-based cathode materials were mostly focused on a redox couple of Fe^{2+}/Fe^{3+}.[18c-f] For instance, MIL-68 was found to accommodate 0.35 Li per Fe atom, or specific capacity of up to 40 mAh/g, which was slightly lower than those of MIL-53. MIL-101, a framework possessing larger pores, is also applicable to a cathode material, showing discharge specific capacity of up to 110 mAh/g with reasonable cyclability (Figure 1.2.3).[18d] Not only preliminary studies, but also examination of detailed electrochemical mechanisms was carried out with MIL-53 using X-ray absorption fine structure (XAFS), extended XAFS (EXAFS)[18e] and theoretical calculation techniques.[18f] Those studies confirmed stable crystal phases with mixed valence states of Fe owing to the flexible framework of MIL-53, but also found that 0.6 Li is the upper limit of its storage and further insertion destabilize the material. Another major class of MOFs for cathodes in lithium ion batteries is Prussian blue and its analogues.[18g-h] The simplicity of the structures of those materials (metal cations are bridged with cyanide), variety of metal compositions are available. However, in general, their capacity and cycle performance were moderate in cathodes of the batteries.

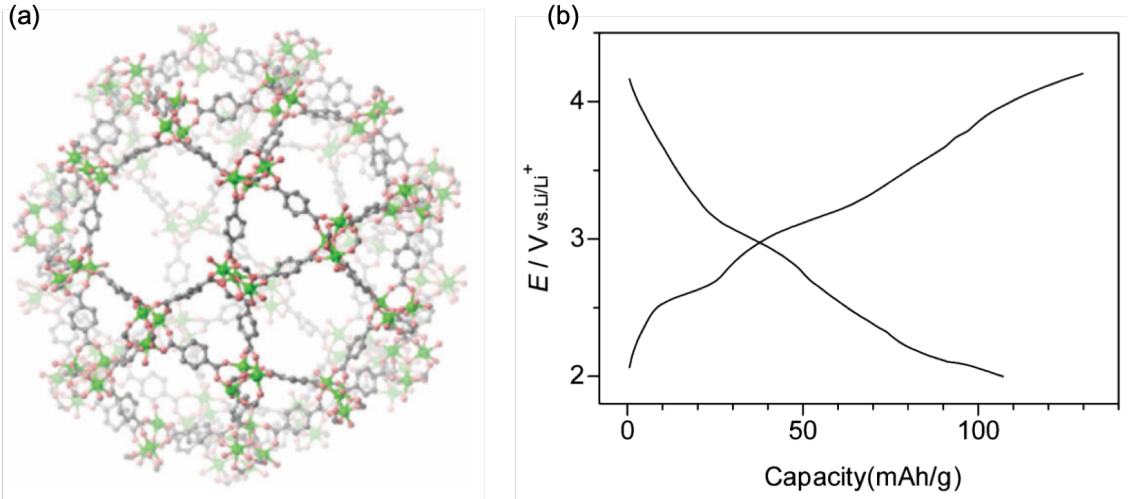

Figure 1.2.3. (a) Structure of MIL-101 and (b) its charge-discharge profile. Adapted with permission from reference 18d. Copyright © Royal Society of Chemistry.

Compared with studies of MOF-based cathode materials, a wider variety of MOFs were investigated as anode materials.[23] The representative examples are $Co_2(OH)_2BDC$ (BDC = 1,4-benzenedicarboxylate),[23a] Mn-1,4-BDC@200 (Figure 1.2.4),[23b] Cu3(BTC)2 (BTC = 1,3,5-benzenetricarboxylate),[23c] and Co-TFBDC (TFBDC = 2,3,5,6-tetrafluoroterephthalic).[23d] The reversible insertion/desertion of Li^+ ions into/from those frameworks takes place based on the ligand-centered redox reactions without contribution from redox couples of metal cations.

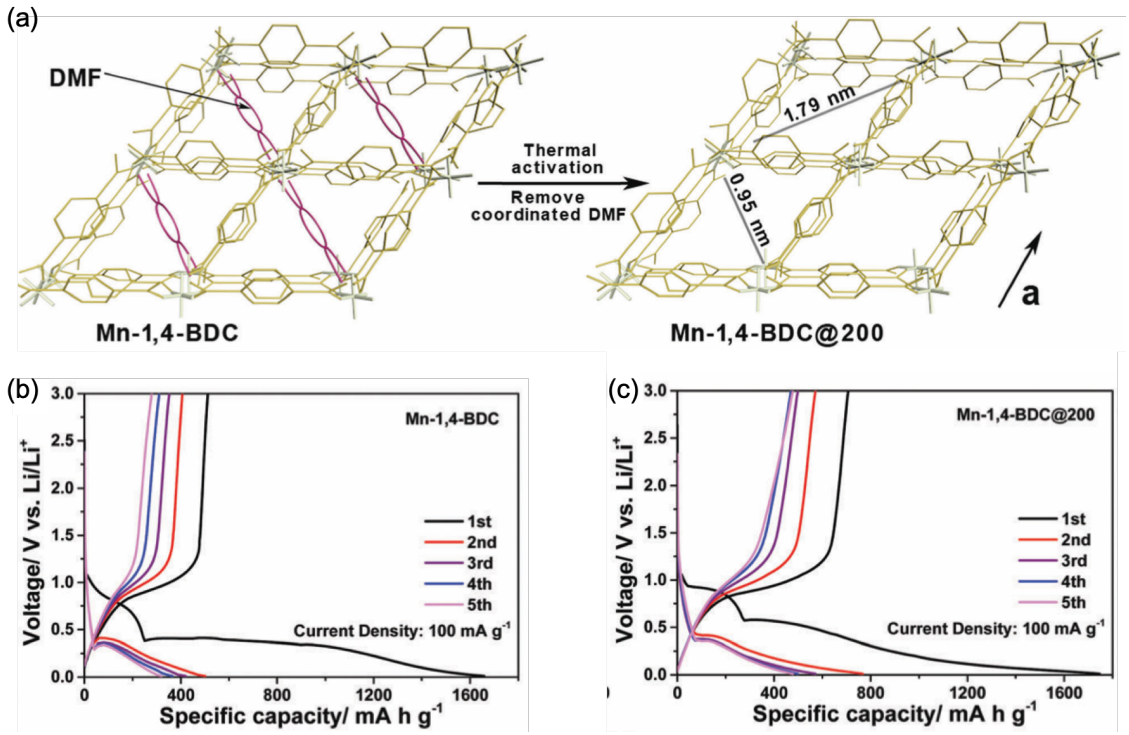

Figure 1.2.4. (a) Structures of Mn-1,4-DBC and DMF-removed Mn-1,4-DBC@200. The charge-discharge profiles of (b) Mn-1,4-DBC and (c) Mn-1,4-DBC@200. Adapted with permission from reference 23b. Copyright © Royal Society of Chemistry.

Several studies have demonstrated that MOFs are promising candidates for energy storage materials, yet some challenging issues remain.[13] At first, electronically insulating nature of typical MOFs causes low rate capability and faster degradation of the materials. In order to access this issue, a lot of efforts have been made by developing composites of MOFs and electronically conductive materials such as graphene.[24] In recent

years, electronically conductive MOFs have been reported as well, a part of which is introduced in the next section. Second, as prepared MOFs often have solvents in pore cavities, and extraction or replacement of them leads to destruction of the frameworks.[1a] Origins of the degradation is not limited only to removal of the solvents, but essential redox processes are also related in many cases. For example, in the case of MOF-based anodes, the materials with ligand-based intercalation often lose crystallinity during cycling, resulting in capacity fading.[23] In spite of the above drawbacks, MOFs are still a promising class of energy storage materials because their properties could essentially be improved by designing appropriate structures.

1.3. Electrically conductive coordination nanosheets

While MOFs are typically insulating, in the last decade, researchers have developed MOFs possessing electronically semi-conductive, or sometimes metallic properties.[25] Thanks to the characteristics, those materials are considered to be promising for various applications that requires charge transport such as electronics, electrocatalysis or electrochemical energy storages. On designing the electronically conductive MOFs, possible strategies are categorized into two ways, through-space and through-bond charge transport.[25] Those strategies succeeded to some extent, and several types of conductive MOFs with three dimensionality have been reported. However, most of them were semiconductors, and thus another approach to improve electronic conductivity was desired.

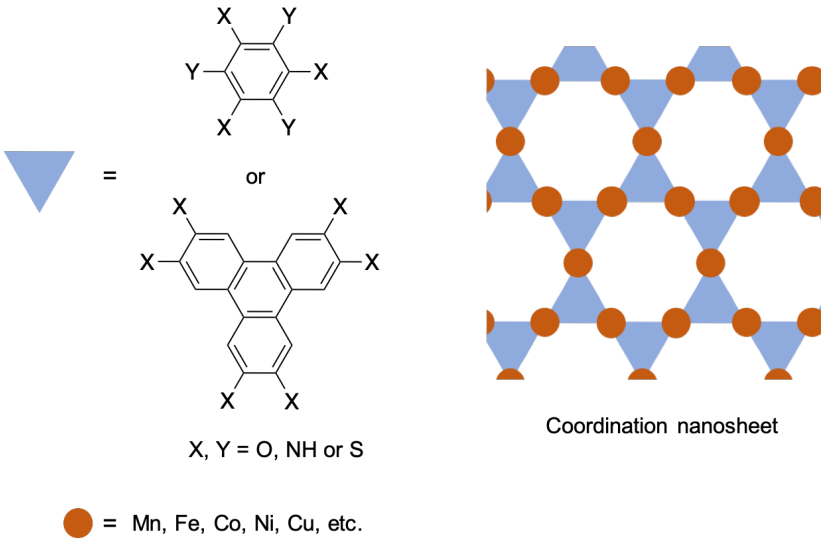

Figure 1.3.1. Structure of electronically conductive coordination nanosheets along the axis vertical to two-dimensional planes.

In 2010s, a novel class of conductive MOFs, which is sometimes termed "coordination nanosheets", has been of great interests because of its unique characteristics.[26-29] Unlike conventional three-dimensional MOFs, coordination nanosheets have an analogous structure of graphene or graphite with two-dimensional anisotropy (Figure 1.3.1). Additionally, organic ligands in the nanosheets have aromatic moieties, the π-conjugations of which are extended to overall structures across metal and ligating groups. Both

the experimental and theoretical studies have revealed that this extended conjugation often offers exceptionally high electronic conductivity.[26-28] All the reported materials in this class have benzene or triphenylene core skeletons with ligating groups of O, N or S.

The earliest study of the highly conductive coordination nanosheet was reported by Kambe *et al.*, in which Ni(II) ions and 1,2,3,4,5,6-benzenehexathiol (BHT) were used to synthesize the nanosheet, NiDT (Figure 1.3.2).[27a] A two-probe electronic conductivity measurement of the as-prepared material displayed conductivity of 0.15 S/cm at 298 K. Furthermore, the following study by the same authors revealed that NiDI increased its conductivity to 1.6×10^2 S/cm via chemical oxidation.[27b] A theoretical calculation found that the electronic band structure of the nanosheet had a metallic feature, which is unusual for MOFs. Huang *et al.* reported that the BHT-based nanosheet with Cu(II) ions (CuBHT) exhibited further higher conductivity of up to 1,580 S/cm at room temperature (Figure 1.3.3).[27c] To the best of my knowledge, to date, this value is the highest among reported MOFs. Additionally, Cu-BHT with improved crystallinity was found to show superconductivity at a temperature below 250 mK.[27d] As the other BHT-based nanosheets, the materials with heavier d^8 metals, Pd and Pt,[27e-f] were also reported, although they did not display conductivity as high as the above examples. Nanosheets with the derivative of BHT, 2,3,6,7,10,11-triphenylenehexathiol (THT), have also been majorly targeted materials. For instance, the THT-based nanosheets with several first-low transition metals (Fe, Co and Ni) were synthesized, respectively, and their catalytic or electronic properties were examined.[27g-h]

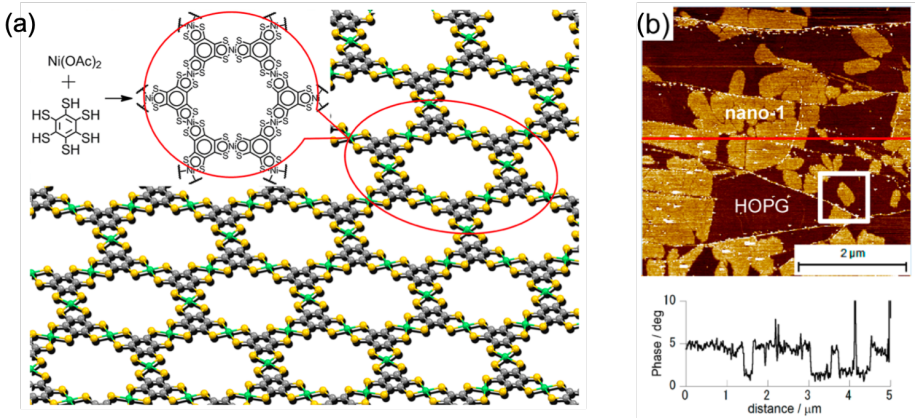

Figure 1.3.2. (a) Structure of NiDT and (b) the AFM image of the film state NiDT. Adapted with permission from reference 27a. Copyright © 2013, American Chemical Society.

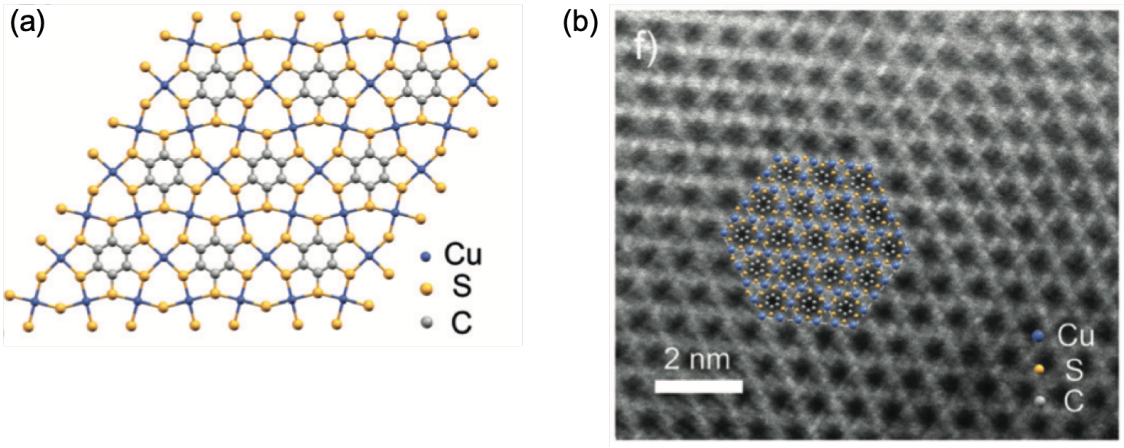

Figure 1.3.3. (a) Structure of CuBHT and (b) its amplified high-resolution TEM image. Differently from NiDT, a S atom in CuBHT coordinates to two Cu atoms. Adapted with permission from rerefence 27c for (a) and 27d for (b). Copyright © 2015, Springer Nature and © 2018 Wiley‐VCH Verlag GmbH & Co. KGaA, Weinheim.

Similarly to the sulfur-containing nanosheets, a family of the nitrogen-based nanosheets were known to possess high electronic conductivity.[28] The early work by Sheberla *et al.*,in which 2,3,6,7,10,11-hexaiminotriphenylene (HITP) and Ni(II) ions were incorporated into the framework, and they observed its electronic conductivity as high as 40 S/cm at room temperature.[28a] The same authors also reported the nanosheet consisting of HITP and Cu(II) ions, which showed slightly lower conductivity but usability for chemiresistive sensing of ammonia.[28b] Bis(diimino)metal coordination nanosheets (MDIs, M = metal), a series of other nitrogen-based nanosheets composed of hexaiminobenzene, have been rapidly developed in these years.[28c-h] The metal species of reported MDIs include Co, Ni, Cu, Fe, Mn and Fe/Mn (mixture), and each was demonstrated to be electronically conductive. A part of the previous studies related to those nanosheets are more detailly described in the following chapters.

Finally, several types of nanosheets synthesized from the oxygen-based ligands, 1,2,3,4,5,6-hexahydroxybenzene or 2,3,6,7,10,11-hexahydroxytriphenylene, have been reported with several transition metals.[29] While these ligands tend to offer good crystallinity, and thus advantageous for unambiguous structure determination, their electronic conductivities are not as high as the other types of nanosheets.

1.4. The aim of this research

Thanks to high electronic conductivity, MDIs offer us an opportunity to employ them for applications requiring charge transport.[28] Furthermore, imine groups sharing aromaticity in the ligand are well-known as redox-active species (Figure 1.4.1 a).[30] Thus, MDIs are expected to be promising candidates for electrochemical energy storage materials in batteries or supercapacitors. In my Ph.D. thesis, MDIs with several metal species were synthesized and electrochemistry-related properties were investigated, aiming at energy storage applications (Figure 1.4.1 b). As metal species, Ni, Co, Cu and Co/Ni (mixture) were adopted to reveal electrochemical properties with respective metals. Associating the chemical structures and emerging properties, the knowledge obtained in this thesis will contribute to rational design of novel energy storage materials with desired functions.

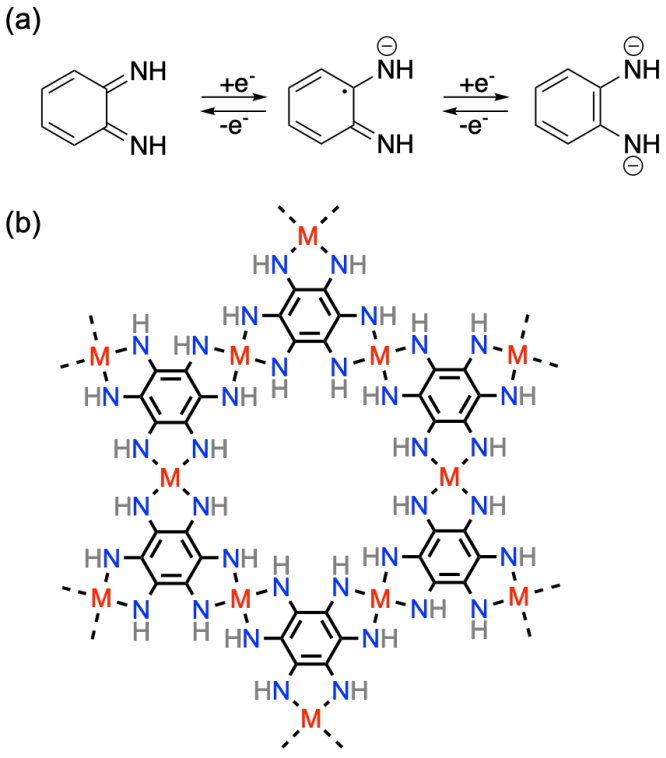

Figure 1.4.1. (a) Redox reactions of 1,2-diiminobenzene. (b) The chemical structure of the targeted material, MDI (M = Ni, Co, Cu or Co/Ni (mixture)).

1.5. References

1. (a) H. Furukawa, K. E. Cordova, M. O'Keeffe, O. M. Yaghi, *Science* **2013**, *341*, DOI 10.1126/science.1230444.
   (b) S. Kitagawa, R. Kitaura, S. I. Noro, *Angew. Chemie - Int. Ed.* **2004**, *43*, 2334–2375.
   (c) J. Lee, O. K. Farha, J. Roberts, K. A. Scheidt, S. T. Nguyen, J. T. Hupp, *Chem. Soc. Rev.* **2009**, *38*, 1450–1459.
   (d) A. G. Slater, A. I. Cooper, *Science* **2015**, *348*, aaa8075.
2. (a) S. Mendiratta, M. Usman, K. L. Lu, *Coord. Chem. Rev.* **2018**, *360*, 77–91.
   (b) K. Sumida, D. L. Rogow, J. A. Mason, T. M. McDonald, E. D. Bloch, Z. R. Herm, T. H. Bae, J. R. Long, *Chem. Rev.* **2012**, *112*, 724–781.
   (c) L. E. Kreno, K. Leong, O. K. Farha, M. Allendorf, R. P. Van Duyne, J. T. Hupp, *Chem. Rev.* **2012**, *112*, 1105–1125.
3. Y. Kinoshita, I. Matsubara, Y. Saito, *Bull. Chem. Soc. Jpn.* **1959**, *32*, 741–747.
4. H. Li, M. Eddaoudi, T. L. Groy, O. M. Yaghi, *J. Am. Chem. Soc.* **1998**, *120*, 8571–8572.
5. H. Li, M. Eddaoudi, M. O'Keeffe, O. M. Yaghi, *Nature* **1999**, *402*, 276–279.
6. (a) H. Furukawa, N. Ko, Y. B. Go, N. Aratani, S. B. Choi, E. Choi, A. Ö. Yazaydin, R. Q. Snurr, M. O'Keeffe, J. Kim, O. M. Yaghi, *Science* **2010**, *329*, 424–428.
   (b) O. K. Farha, I. Eryazici, N. C. Jeong, B. G. Hauser, C. E. Wilmer, A. A. Sarjeant, R. Q. Snurr, S. T. Nguyen, A. Ö. Yazaydin, J. T. Hupp, *J. Am. Chem. Soc.* **2012**, *134*, 15016–15021.
   (c) O. K. Farha, A. Ö. Yazaydin, I. Eryazici, C. D. Malliakas, B. G. Hauser, M. G. Kanatzidis, S. T. Nguyen, R. Q. Snurr, J. T. Hupp, *Nat. Chem.* **2010**, *2*, 944–948.
7. (a) H. Deng, S. Grunder, K. E. Cordova, C. Valente, H. Furukawa, M. Hmadeh, F. Gandara, A. C. Whalley, Z. Liu, S. Asahina, et al., *Science* **2012**, *336*, 1018–1023.
   (b) N. L. Rosi, J. Kim, M. Eddaoudi, B. Chen, M. O'Keeffe, O. M. Yaghi, *J. Am. Chem. Soc.* **2005**, *127*, 1504–1518.
8. T. M. McDonald, J. A. Mason, X. Kong, E. D. Bloch, D. Gygi, A. Dani, V. Crocellà, F. Giordanino, S. O. Odoh, W. S. Drisdell, et al., *Nature* **2015**, *519*, 303–308.
9. (a) E. D. Bloch, W. L. Queen, R. Krishna, J. M. Zadrozny, C. M. Brown, J. R. Long, *Science* **2012**, *335*, 1606–1610.

(b) Z. R. Herm, B. M. Wiers, J. A. Mason, J. M. van Baten, M. R. Hudson, P. Zajdel, C. M. Brown, N. Masciocchi, R. Krishna, J. R. Long, *Science* **2013**, *340*, 960–964.

(c) S. Yang, A. J. Ramirez-Cuesta, R. Newby, V. Garcia-Sakai, P. Manuel, S. K. Callear, S. I. Campbell, C. C. Tang, M. Schröder, *Nat. Chem.* **2015**, *7*, 121–129.

10. (a) M. Fujita, S. Washizu, K. Ogura, Y. J. Kwon, *J. Am. Chem. Soc.* **1994**, *116*, 1151–1152.

(b) K. Schlichte, T. Kratzke, S. Kaskel, *Microporous Mesoporous Mater.* **2004**, *73*, 81–88.

(c) L. Alaerts, E. Séguin, H. Poelman, F. Thibault-Starzyk, P. A. Jacobs, D. E. De Vos, *Chem. - A Eur. J.* **2006**, *12*, 7353–7363.

11. M. E. Davis, *Acc. Chem. Res.* **1993**, *26*, 111–115.

12. S. S. Y. Chui, S. M. F. Lo, J. P. H. Charmant, A. G. Orpen, I. D. Williams, *Science* **1999**, *283*, 1148–1150.

13. D. M. D'Alessandro, *Chem. Commun.* **2016**, *52*, 8957–8971.

14. (a) K. Mizushima, P. C. Jones, P. J. Wiseman, J. B. Goodenough, *Mater. Res. Bull.* **1980**, *15*, 783–789.

(b) T. Ohzuku, A. Ueda, M. Nagayama, Y. Iwakoshi, H. Komori, *Electrochim. Acta* **1993**, *38*, 1159–1167.

(c) M. M. Thackeray, P. J. Johnson, L. A. de Picciotto, P. G. Bruce, J. B. Goodenough, *Mater. Res. Bull.* **1984**, *19*, 179–187.

(d) F. Shi, L. Li, X. L. Wang, C. D. Gu, J. P. Tu, *RSC Adv.* **2014**, *4*, 41910–41921.

15. S. R. Ovshinsky, M. A. Fetcenko, J. Ross, *Science* **1993**, *260*, 176–181.

16. (a) A. K. Padhi, K. S. Nanjundaswamy, C. Masquelier, S. Okada, J. B. Goodenough, *J. Electrochem. Soc.* **1997**, *144*, 1609-1613.

(b) Z. Gong, Y. Yang, *Energy Environ. Sci.* **2011**, *4*, 3223–3242.

17. R. Zhao, Z. Liang, R. Zou, Q. Xu, *Joule* **2018**, *2*, 2235–2259.

18. (a) X. Li, F. Cheng, S. Zhang, J. Chen, *J. Power Sources* **2006**, *160*, 542–547.

(b) G. Férey, F. Millange, M. Morcrette, C. Serre, M. L. Doublet, J. M. Grenèche, J. M. Tarascon, *Angew. Chemie - Int. Ed.* **2007**, *46*, 3259–3263.

(c) A. Fateeva, P. Horcajada, T. Devic, C. Serre, J. Marrot, J. M. Grenèche, M. Morcrette, J. M. Tarascon, G. Maurin, G. Férey, *Eur. J. Inorg. Chem.* **2010**, *68*, 3789–

3794.

(d) T. Yamada, K. Shiraishi, H. Kitagawa, N. Kimizuka, *Chem. Commun.* **2017**, *53*, 8215–8218.

(e) G. de Combarieu, S. Hamelet, F. Millange, M. Morcrette, J. M. Tarascon, G. Férey, R. I. Walton, *Electrochem. commun.* **2009**, *11*, 1881–1884.

(f) C. Combelles, M. Ben Yahia, L. Pedesseau, M. L. Doublet, *J. Power Sources* **2011**, *196*, 3426–3432.

(g) D. Asakura, M. Okubo, Y. Mizuno, T. Kudo, H. Zhou, K. Ikedo, T. Mizokawa, A. Okazawa, N. Kojima, *J. Phys. Chem. C* **2012**, *116*, 8364–8369.

(h) M. Okubo, D. Asakura, Y. Mizuno, J. D. Kim, T. Mizokawa, T. Kudo, I. Honma, *J. Phys. Chem. Lett.* **2010**, *1*, 2063–2071.

19. (a) Y. Lu, L. Wang, J. Cheng, J. B. Goodenough, *Chem. Commun.* **2012**, *48*, 6544–6546.

(b) L. Wang, Y. Lu, J. Liu, M. Xu, J. Cheng, D. Zhang, J. B. Goodenough, *Angew. Chemie - Int. Ed.* **2013**, *52*, 1964–1967.

20. Y. Zheng, S. Zheng, H. Xue, H. Pang, *J. Mater. Chem. A* **2019**, *7*, 3469–3491.

21. D. Wu, Z. Guo, X. Yin, Q. Pang, B. Tu, L. Zhang, Y. G. Wang, Q. Li, *Adv. Mater.* **2014**, *26*, 3258–3262.

22. B. M. Wiers, M. L. Foo, N. P. Balsara, J. R. Long, *J. Am. Chem. Soc.* **2011**, *133*, 14522–14525.

23. (a) L. Gou, L. M. Hao, Y. X. Shi, S. L. Ma, X. Y. Fan, L. Xu, D. L. Li, K. Wang, *J. Solid State Chem.* **2014**, *210*, 121–124.

(b) H. Hu, X. Lou, C. Li, X. Hu, T. Li, Q. Chen, M. Shen, B. Hu, *New J. Chem.* **2016**, *40*, 9746–9752.

(c) S. Maiti, A. Pramanik, U. Manju, S. Mahanty, *Microporous Mesoporous Mater.* **2016**, *226*, 353–359.

(d) X. Lou, X. Hu, C. Li, Y. Ning, Q. Chen, M. Shen, B. Hu, *New J. Chem.* **2017**, *41*, 1813–1819.

24. M. Zhu, H. Zhou, J. Shao, J. Feng, A. Yuan, *J. Alloys Compd.* **2018**, *749*, 811–817.

25. L. Sun, M. G. Campbell, M. Dincə, *Angew. Chemie - Int. Ed.* **2016**, *55*, 3566–3579.

26. R. Sakamoto, K. Takada, T. Pal, H. Maeda, T. Kambe, H. Nishihara, *Chem. Commun.* **2017**, *53*, 5781–5801.
27. (a) T. Kambe, R. Sakamoto, K. Hoshiko, K. Takada, M. Miyachi, J. H. Ryu, S. Sasaki, J. Kim, K. Nakazato, M. Takata, et al., *J. Am. Chem. Soc.* **2013**, *135*, 2462–2465.
(b) T. Kambe, R. Sakamoto, T. Kusamoto, T. Pal, N. Fukui, K. Hoshiko, T. Shimojima, Z. Wang, T. Hirahara, K. Ishizaka, et al., *J. Am. Chem. Soc.* **2014**, *136*, 14357–14360.
(c) X. Huang, P. Sheng, Z. Tu, F. Zhang, J. Wang, H. Geng, Y. Zou, C. A. Di, Y. Yi, Y. Sun, et al., *Nat. Commun.* **2015**, *6*, 6–13.
(d) X. Huang, S. Zhang, L. Liu, L. Yu, G. Chen, W. Xu, D. Zhu, *Angew. Chemie - Int. Ed.* **2018**, *57*, 146–150.
(e) T. Pal, T. Kambe, T. Kusamoto, M. L. Foo, R. Matsuoka, R. Sakamoto, H. Nishihara, *Chempluschem* **2015**, *80*, 1255–1258.
(f) T. Pal, S. Doi, H. Maeda, K. Wada, C. M. Tan, N. Fukui, R. Sakamoto, S. Tsuneyuki, S. Sasaki, H. Nishihara, *Chem. Sci.* **2019**, *10*, 5218–5225.
(g) R. Dong, P. Han, H. Arora, M. Ballabio, M. Karakus, Z. Zhang, C. Shekhar, P. Adler, P. S. Petkov, A. Erbe, et al., *Nat. Mater.* **2018**, *17*, 1027–1032.
(h) A. J. Clough, J. M. Skelton, C. A. Downes, A. A. De La Rosa, J. W. Yoo, A. Walsh, B. C. Melot, S. C. Marinescu, *J. Am. Chem. Soc.* **2017**, *139*, 10863–10867.
28. (a) D. Sheberla, L. Sun, M. A. Blood-Forsythe, S. Er, C. R. Wade, C. K. Brozek, A. Aspuru-Guzik, M. Dincă, *J. Am. Chem. Soc.* **2014**, *136*, 8859–8862.
(b) M. G. Campbell, D. Sheberla, S. F. Liu, T. M. Swager, M. Dincă, *Angew. Chemie - Int. Ed.* **2015**, *54*, 4349–4352.
(c) N. Lahiri, N. Lotfizadeh, R. Tsuchikawa, V. V. Deshpande, J. Louie, *J. Am. Chem. Soc.* **2017**, *139*, 19–22.
(d) J. H. Dou, L. Sun, Y. Ge, W. Li, C. H. Hendon, J. Li, S. Gul, J. Yano, E. A. Stach, M. Dincă, *J. Am. Chem. Soc.* **2017**, *139*, 13608–13611.
(e) D. Feng, T. Lei, M. R. Lukatskaya, J. Park, Z. Huang, M. Lee, L. Shaw, S. Chen, A. A. Yakovenko, A. Kulkarni, et al., *Nat. Energy* **2018**, *3*, 30–36.
(f) E. J. H. Phua, K. H. Wu, K. Wada, T. Kusamoto, H. Maeda, J. Cao, R. Sakamoto, H. Masunaga, S. Sasaki, J. W. Mei, et al., *Chem. Lett.* **2018**, *47*, 126–129.

(g) K. Wada, K. Sakaushi, S. Sasaki, H. Nishihara, *Angew. Chemie - Int. Ed.* **2018**, *57*, 8886–8890.

(h) S. S. Shinde, C. H. Lee, J. Y. Jung, N. K. Wagh, S. H. Kim, D. H. Kim, C. Lin, S. U. Lee, J. H. Lee, *Energy Environ. Sci.* **2019**, *12*, 727–738.

29. (a) J. Park, A. C. Hinckley, Z. Huang, D. Feng, A. A. Yakovenko, M. Lee, S. Chen, X. Zou, Z. Bao, *J. Am. Chem. Soc.* **2018**, *140*, 14533–14537.

(b) M. Hmadeh, Z. Lu, Z. Liu, F. Gándara, H. Furukawa, S. Wan, V. Augustyn, R. Chang, L. Liao, F. Zhou, et al., *Chem. Mater.* **2012**, *24*, 3511–3513.

30. D. Herebian, E. Bothe, F. Neese, T. Weyhermüller, K. Wieghardt, *J. Am. Chem. Soc.* **2003**, *125*, 9116–9128.

Chapter 2

Synthesis of bis(diimino)nickel coordination nanosheet (NiDI) and its electrochemical properties as an electrode material in a secondary battery

2.1. Introduction

The nickel complexes synthesized from o-phenylene diamine or its derivatives ([Ni-N_4] type complexes) are known to have unique electronic states (Figure 2.1.1a).[1] When those ligands are embedded in complexes, they behave as non-innocent ligands: they are capable of taking several redox states in addition to the metal centers (Figure 2.1.1b). Owing to the characteristic, [Ni-N_4] type complexes often show multi-step redox state transitions depending on electrochemical potentials (Figure 2.1.1c,d). This unique property has attracted interests for several decades, and a lot of studies have challenged to clarify the mechanisms of the electrochemical reactions by combination of electrochemical and other measurement techniques such as UV-vis absorption spectroscopy or electron paramagnetic resonance spectroscopy. Furthermore, by modifying the structure of *o*-phenylene diamine, various [Ni-N_4] type complexes have been synthesized to investigate influence of the ligand structures on their electrochemical properties as well as their structure geometries.

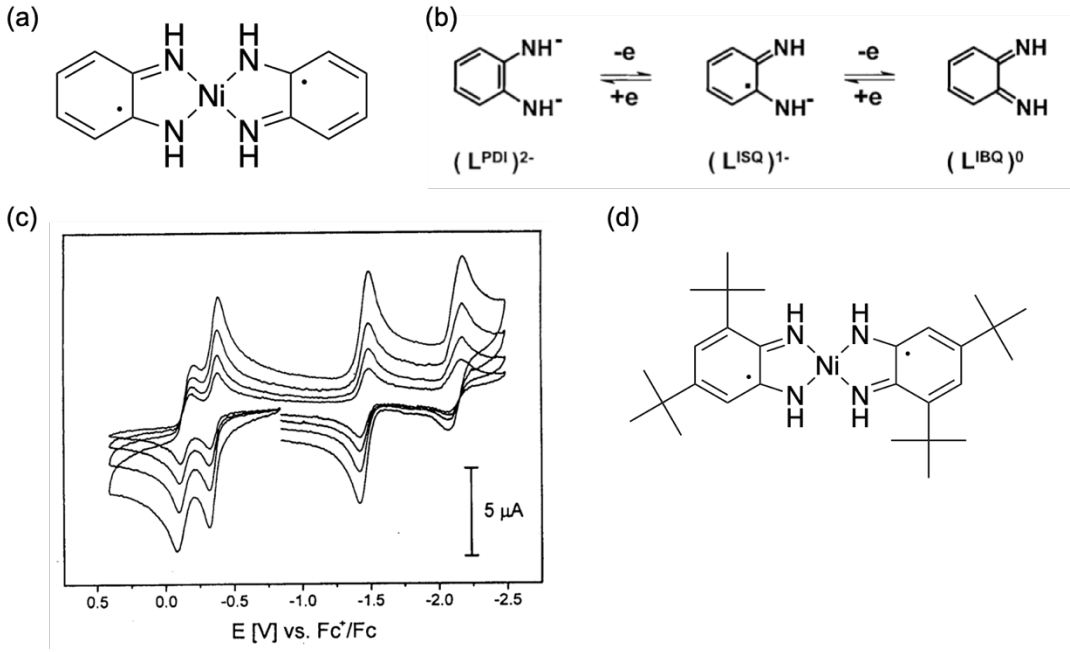

Figure 2.1.1. (a) [Ni-N_4] type complex synthesized from *o*-phenylene diamine. (b) Reaction scheme of the redox reactions of 1,2-bis(diimino)benzene. (c) Cyclic voltammogram of the compound shown in (d), being measured in 0.1 M [N(*n*-Bu)$_4$]BF_4/acetonitrile at scan rates 50, 100, 200, 400 mV/s. Adapted with permission from reference 1a for (b)-(d). Copyright © 2003 American Chemical Society.

In recent years, the two-dimensional coordination nanosheet consisting of Ni(II) ions and 2,3,6,7,10,11-hexaiminotriphenylene was reported (Figure 2.1.2a).[2] Thanks to the electron-

delocalized structure of the [Ni-N_4] complex and also the aromatic triphenylene moiety, electronic conductivity of the material reached up to 40 S/cm at room temperature (Figure 2.1.2b).[2a] In another study, the same authors reported that this material can be applicable as an electrode material in a supercapacitor, in which it marked high areal capacitance and long lifecycles, successfully demonstrating the advantages of the conductive nature and the porous structure (Figure 2.1.2c).[2b]

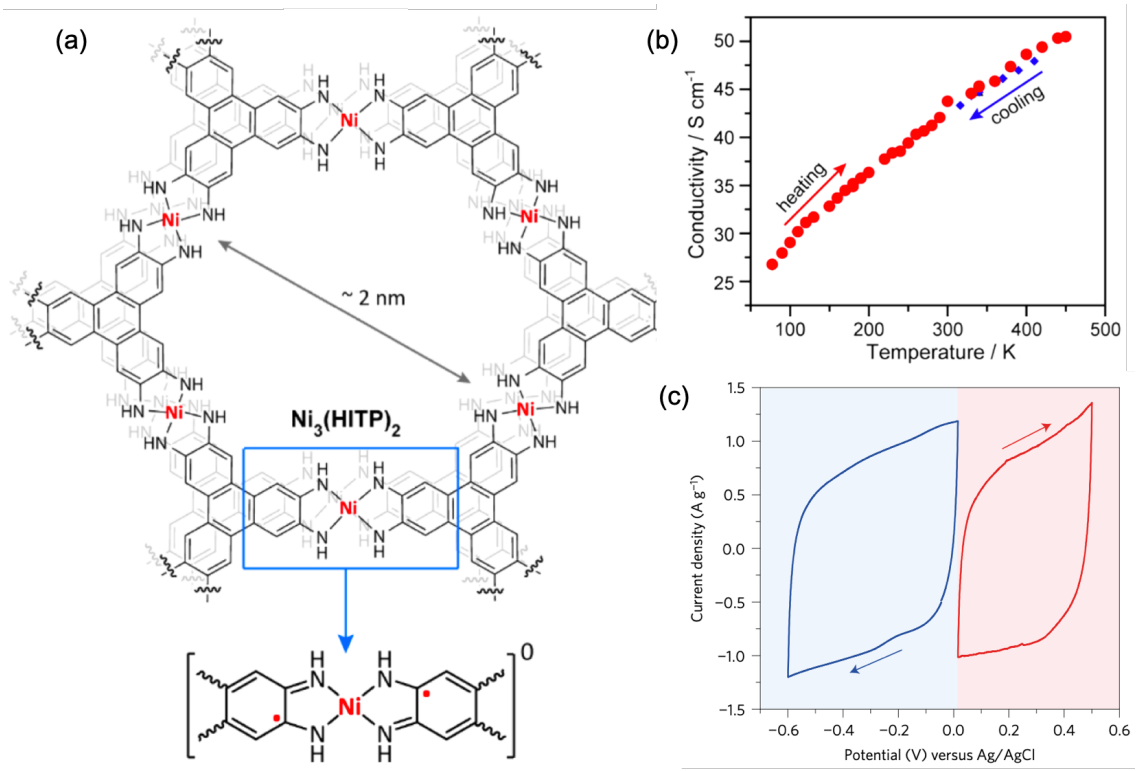

Figure 2.1.2. (a) Coordination nanosheet consisting of Ni(II) ions and 2,3,6,7,10,11-hexaiminotriphenylene. (b) The temperature-dependent electronic conductivity of the material and (c) the cyclic voltammograms in 1 M TEA•BF_4/acetonitrile at scan rate of 10 mV/s. Adapted with permission from reference 2a for (a) and (b), and from reference 2b for (c). Copyright © 2014, American Chemical Society and © 2016, Springer Nature.

As a series of the coordination nanosheet which have [Ni-N_4] type complex skeletons, more recently, the material consisting of hexaiminobenzene was reported from several groups.[3] This bis(diimino)nickel coordination nanosheet (NiDI) are theoretically predicted to have metallic nature on electronic conductivity owing to the delocalized electronic states on the two-dimensional layers (Figure 2.1.3).[3b,d] In fact, the experimentally obtained conductivity was ~ 6 S/cm,[3b] which was quite high as a family of metal-organic frameworks. Moreover, in an aque-

ous supercapacitor, NiDI was found possess high volumetric and areal capacitance as an electrode material.[3c] Based on the characteristics of [Ni-N_4] type complexes exhibiting multi-step redox reactions and the high electronic conductivity, NiDI is expected to be a promising electrode material in a secondary battery which requires both charge-storage and charge-transport functions. However, application of NiDI for secondary batteries has not been studied yet, and its electrochemistry-related properties have not been well-understood.

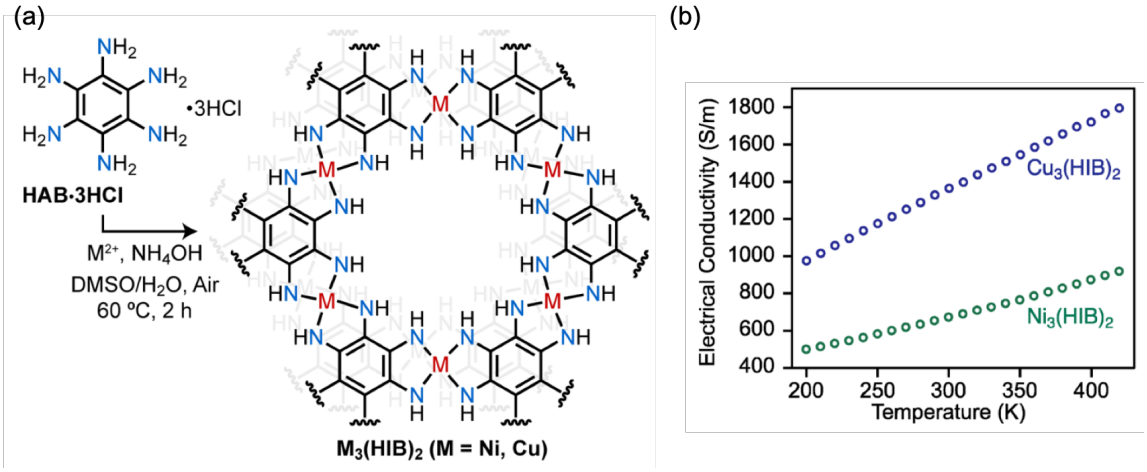

Figure 2.1.3. (a) Reaction scheme of the synthesis of NiDI. (b) The temperature-dependent electronic conductivity of the material. Adapted with permission from reference 3b. Copyright © 2017, American Chemical Society.

In this study, NiDI was synthesized and its electrochemical properties including an energy storage function were investigated. The mechanisms of its electrochemical behaviors were revealed by combination of electrochemical, spectroscopic and theoretical techniques.

2.2. Results and discussion

2.2.1 Synthesis and characterization

NiDI was synthesized via the complexation of hexaaminobenzene tetrahydrochrolide (HAB•3HCl) and nickel(II) acetate tetrahydrate, as shown in Scheme 2.2.1. HAB•3HCl was prepared following the literatures.[3b] The reactions of the NiDI formation include mainly three steps: deprotonation, oxidation of the ligand and the complexation with Ni(II) ions that exists as ammonia complexes in the solution. According to the literature, the first reaction is the coordination of HCl free HAB with Ni(II) ions, and then successive deprotonation on the amino-group and its oxidation subsequently take place.[3c] Until now, by using the characteristic of the reaction promoted by the ligand oxidation, two of the synthesis methods of NiDI have been developed that are the synthesis using oxygen molecules in air as oxidants[3b,d] and the electrochemical synthesis where the reaction occurs on an electrode.[3d] In this study, the former method was employed as it allowed to easily prepare large amount of the product. The preparation procedure is depicted in Figure 2.2.1, which yielded the black powder product (~ 80%).

Scheme 2.2.1. Preparation of NiDI from HAB•3HCl and Ni(II) ions

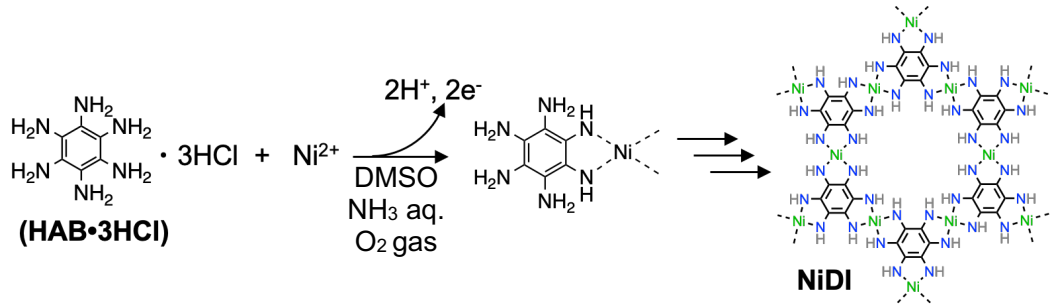

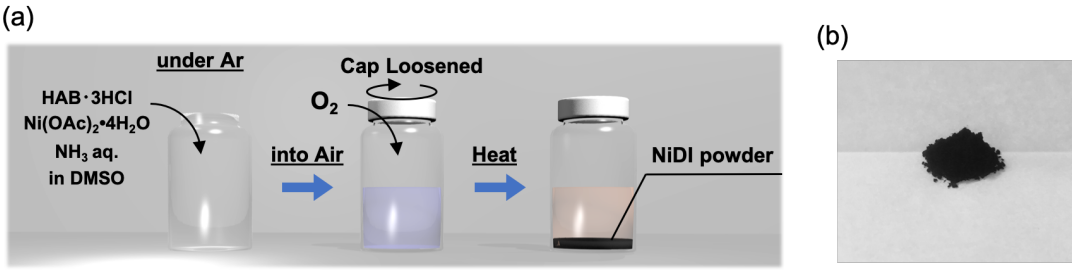

Figure 2.2.1. (a) Schematic illustration of the synthesis method of NiDI using oxygen molecules in air, and (b) the photo of the resulting NiDI power.

The microscopic characterization of the NiDI powder was carried out by high resolution transmission electron microscopy (HR-TEM). In the observation, a highly crystalline phase was observed, and the diameter of each crystal domain size was about 30 nm (Figure 2.2.3). Fast Fourier transform analysis of the selected area clearly showed the hexagonal pattern, suggesting the honeycomb lattice of the material. The periodic pattern in the higher resolution image matched well with the expected structure of NiDI.

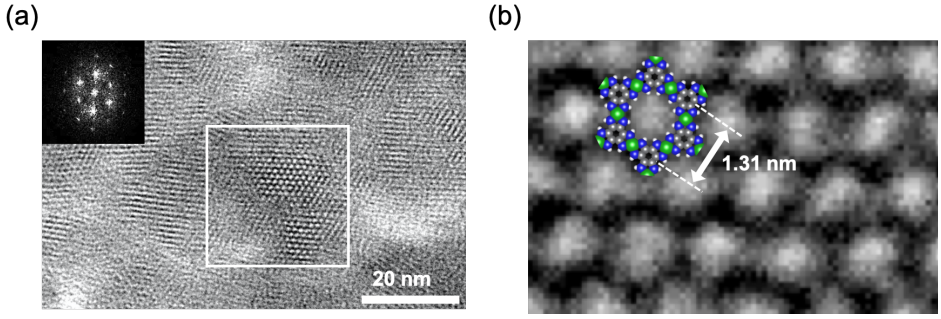

Figure 2.2.3. (a) HR-TEM image of the NiDI powder. The inset is the image obtained by fast Fourier transform analysis of the selected area indicated by the white lines. (b) The higher-resolution TEM image of NiDI, on which the expected partial structure of NiDI is illustrated (N: blue, C: gray, H: white and Ni: green).

The powder X-ray diffraction (PXRD) measurement conducted by synchrotron radiation also showed the crystalline structure of NiDI. In order to determine the crystal structure of NiDI, the experimentally obtained diffraction pattern was simulated with several model structures of NiDI. The experimental result was reasonably reproduced by the AA stacking (eclipsed) structure rather than the other models such as an AB stacking (staggered) structure, which agreed with the literatures (Figure 2.2.4).[3c-d] The corresponding space group of the simulation model was P6/mmm, and the experimentally obtained lattice parameters were a = 13.11 Å and c = 3.27 Å. In addition to these simulations, when H_2O molecules were placed in pores of the AA stacking structure, the pattern simulated with the model showed better consistency with the experimental pattern, indicating existence of solvents such as H_2O or other species in the pores.

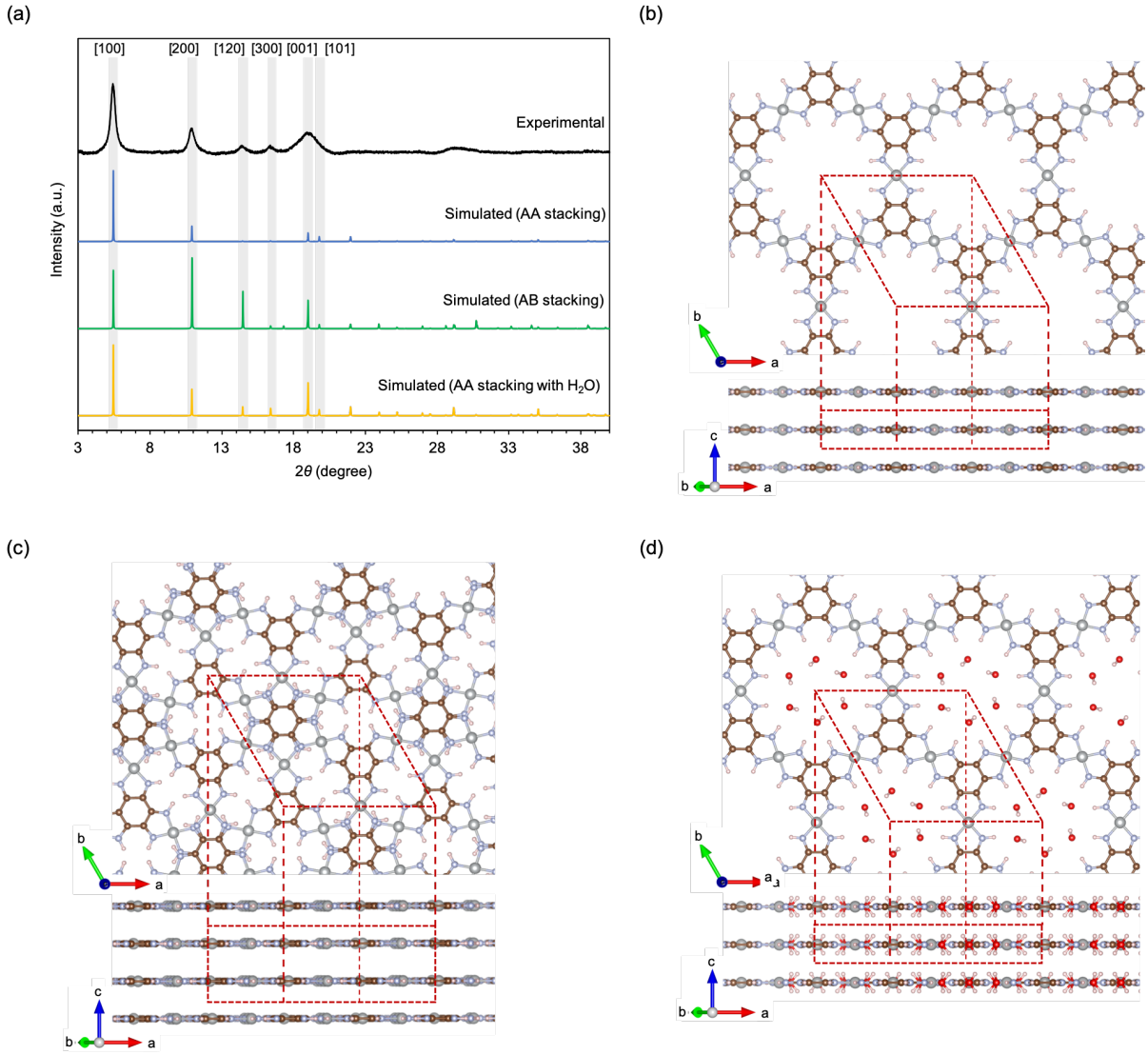

Figure 2.2.4. (a) Experimentally obtained PXRD pattern of NiDI and the simulated patterns with (b) the AA stacking model, (c) the AB stacking model and (d) the AA stacking model with H_2O molecules. The unit cell of the simulation model is defined by the red dash lines. Copyright © 2018 Wiley‐VCH Verlag GmbH & Co. KGaA, Weinheim.

The chemical bonds in the material were characterized by infrared (IR) spectroscopy and Raman spectroscopy (Figure 2.2.5). In the IR spectra, the signals appeared in two regions that were over 3000 cm^{-1} and 1700 cm^{-1}. At higher frequency region, the signals can be deconvoluted into two broad peaks at 3430 cm^{-1} and 3250 cm^{-1}. The former peak was derived from O-H stretching from water molecules and the latter was from N-H stretching from the ligand. The peak of water did not disappear even after heating at 120°C under vacuum for 10 min. Thus, those molecules were strongly absorbed thorough some chemical interaction with the NiDI

framework, most possibly hydrogen bonding with imine function groups. On the other hand, in the frequency region below 1700 cm^{-1}, the peaks mainly derived from C-N and C-C stretching vibrations were observed. Although explicit assignment of those peaks is difficult due to their complexity, the vibration at 1630 cm^{-1} could be assigned to vibration of C-N stretching followed by the other vibration modes. In the Raman spectrum, the symmetric vibration of the chelate rings was observed at 465 cm^{-1} and 630 cm^{-1},[4] and the aromatic-centered vibration was detected around 1500 cm^{-1}. These characterizations clearly indicate the successful formation of the expected coordination networks.

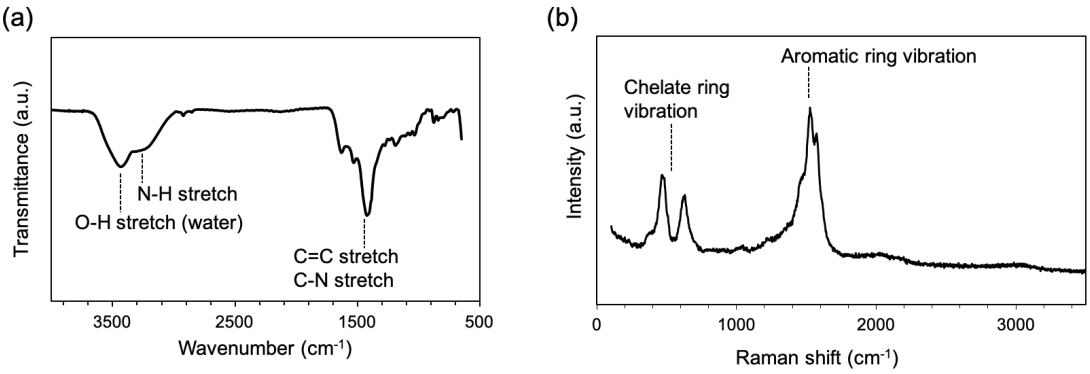

Figure 2.2.5. (a) IR and (b) Raman spectra of NiDI.

The electronic states of N, C and Ni atoms on NiDI were then investigated by X-ray photoelectron spectroscopy (XPS) measurements. In N 1s region, the spectrum showed the peak which was deconvoluted into three peaks (Figure 2.2.6a). The peaks at 398.1 eV (red) and 399.3 eV (yellow) were originated from –(C–NH)$^-$ –Ni and –C=NH-Ni species, respectively.[5] This result suggests that the all imine groups in the ligand were not identical but they take charge-localized states, unlike symmetric [Ni-N_4] type complexes. A content ratio of the above species was calculated to be almost 1 : 1, revealing that the pristine NiDI was at a non-charged state. The peaks at higher binding energies (green and blue) were probably originated from the nitrogen species around the metal vacant sites, in which the peaks could be assigned to ammonium cations, nitroso groups or further oxidized species (Figure 2.2.6b).[6] Analysis of the C 1s region was more complicated due to the signals from adventitious carbon in addition to the NiDI sample. The deconvolution, with consideration of the adventitious carbon, gave four kinds of C atoms, where the C atoms in –(C–NH)$^-$ –Ni and –C=NH-Ni were observed respectively at 285.7 and 287.2 eV (Figure 2.2.6c,d).[5] The content amount of those species were almost equal, which

was reasonably consistent with the result of the N 1s spectrum. The spectrum of Ni 2p3/2 region indicated the existence of mostly one Ni species at 855.0 eV and the slight amount of another type of Ni atoms at 856.2 eV (Figure 2.2.6e,f), in which both of the peaks indicated divalent states of the Ni atoms. While the former atoms were derived from the non-charged complex units, the latter was possibly from the partially oxidized complexes.[7]

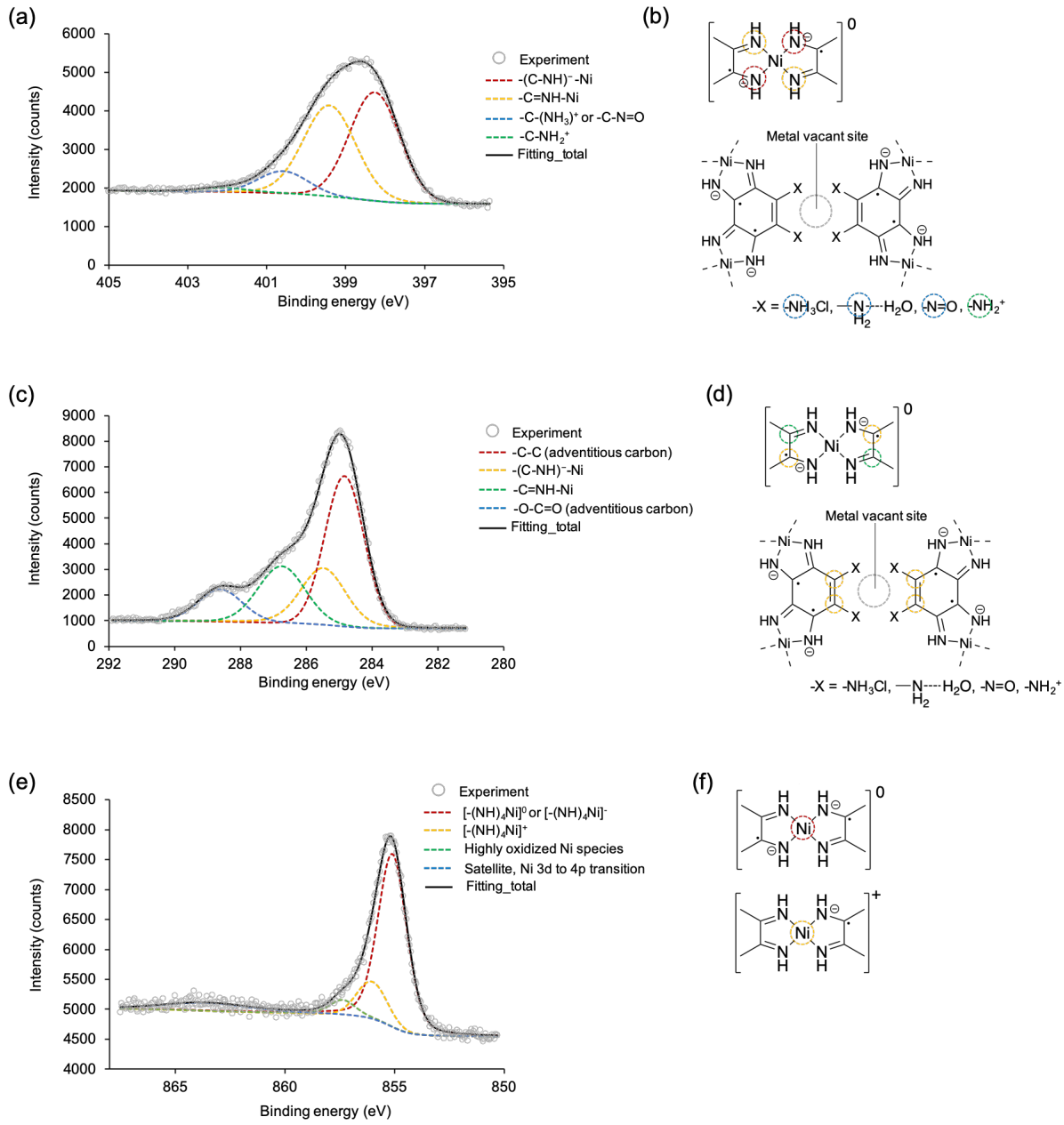

Figure 2.2.6. X-ray photoelectron spectra of NiDI in (a) N1s, (c) C 1s and (e) Ni 2p3/2 regions. The possible atomic species represented by the respective deconvoluted peaks are shown in (b), (d) and (f), in which the atoms were indicated by the corresponding colors of the respective peaks.

2.2.2 Fundamental electrochemical properties

For investigation of the electrochemical properties of NiDI, NiDI-containing electrodes were prepared first by mixing NiDI with multi-walled carbon nanotube (MWCNT) and polyvinylidene difluoride (PVdF), which were pasted on aluminum foil. The fabricated electrode was then used as a cathode in a lithium battery cell as shown in Figure 2.2.7. As the electrolyte, 1 M $LiPF_6$ in mixture of ethylene carbonate and diethyl carbonate (3:7) was used, which is a typical electrolyte used in lithium ion batteries. In this thesis, all potentials are discussed with V vs. Li^+/Li unless otherwise noted.

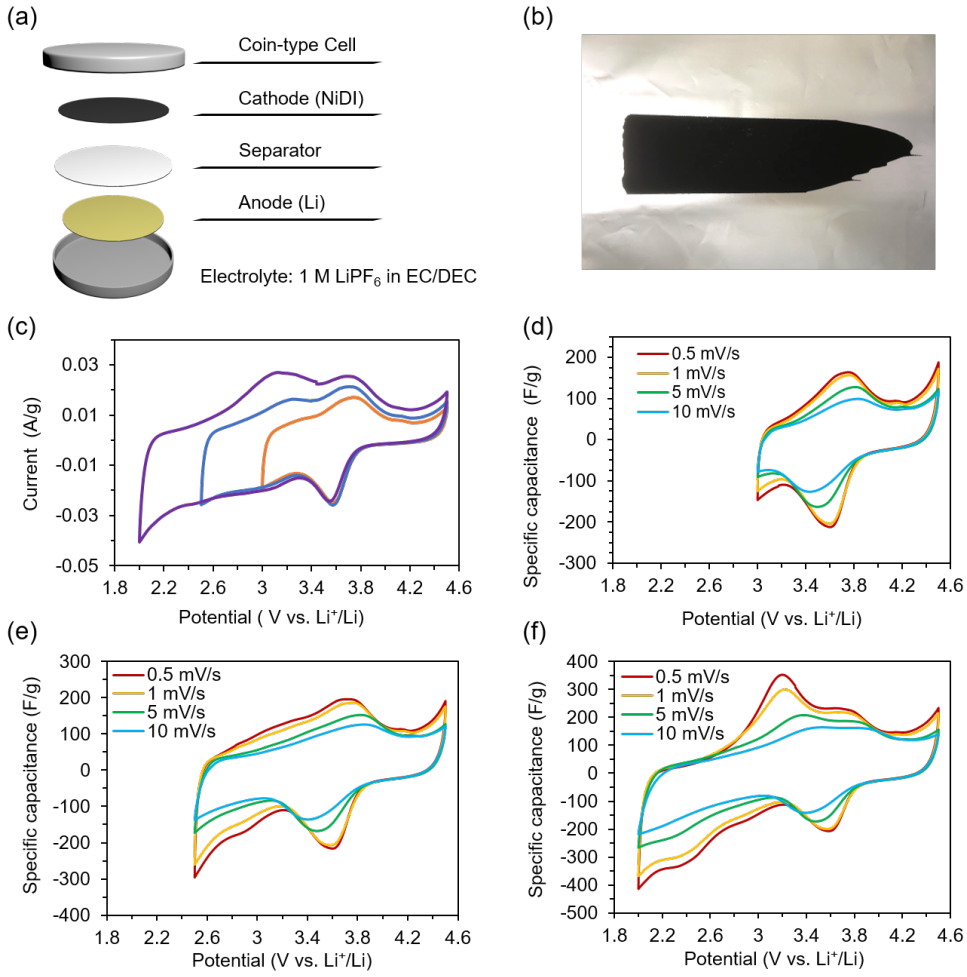

Figure 2.2.7. (a) Schematic image of cell configuration of the lithium battery used for the electrochemical measurements. (b) The cathode containing NiDI, MWCNT and PVdF, which were placed on aluminum foil. (c) The CVs of NiDI at 0.1 mV/s in several potential windows and (d-f) at several scan rates. Copyright © 2018 Wiley‐VCH Verlag GmbH & Co. KGaA, Weinheim.

The cyclic voltammograms (CVs) of the NiDI electrode are given in Figure 2.2.7. The initial open circuit potential of NiDI was 3.15 V. Then during scan in the potential window of 3.0 ~ 4.5 V, the CV exhibited a pair of redox peaks at the cathodic potential of 3.73 V and the anodic potential of 3.56 V. Because those potentials were more positive than the initial open circuit potential of non-charged NiDI, the redox peaks correspond to the electrochemical transition between non-charged and oxidized states of NiDI, being accompanied by insertion/desertion of PF_6^- counteranion.[8] When the negative limit of the potential window was extended to 2.5 V, the CV showed broadly ranging anodic current below 3.0 V and a new cathodic peak at 3.21 V. These redox waves could be assigned to the redox state transition between the non-charged and reduced states of NiDI with Li^+ ion insertion/desertion.[8] The current intensity of these redox waves was further intensified in the more extended potential window (2.0 ~ 4.5 V). In addition to those redox waves, all the CVs showed the irreversible cathodic current near 4.5 V, which was derived from decomposition of the electrolyte. The CVs at various scan rates in Figure 2.2.7c showed that the hysteresis of each pair of redox waves increased at higher rates, which was probably caused by the solid-state diffusion of the counter-ions.

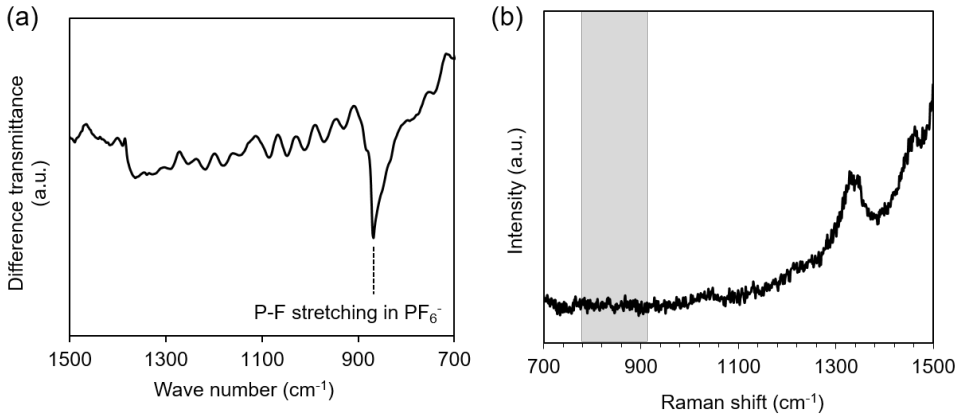

Figure 2.2.8. (a) Difference IR spectrum and (b) the difference Raman spectrum between the oxidized and non-charged NiDIs. The ν_5 vibration mode of PF_6^- appeared in the IR spectrum at 868 cm^{-1} whereas the same frequency region of the Raman spectrum did not show obvious peaks. Copyright © 2018 Wiley‐VCH Verlag GmbH & Co. KGaA, Weinheim.

NiDI at the oxidized state was then investigated with Raman and IR spectroscopy to characterize the PF_6^--inserted material (Figure 2.2.8). The IR spectrum showed the peak corresponding to the ν_5 vibration mode of a PF_6^- ion with distorted symmetry while no peak was observed in the same frequency region of the Raman spectrum.[9] These results confirmed the

successful insertion of PF_6^- ion in the framework. This unique multielectron transfer behavior associated with both cation and anion insertion are not commonly observed in solid-state electrochemistry, and only a few examples have been reported for MOF-based materials.

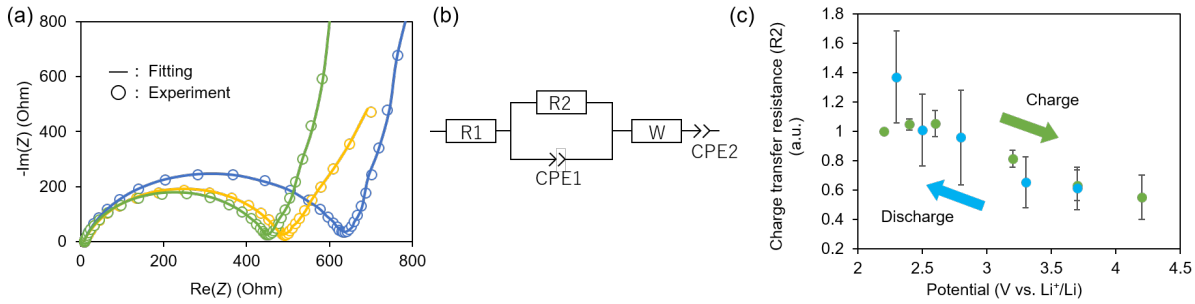

Figure 2.2.9. (a) The Nyquist plots of NiDI measured at 2.2 V (blue), 3.2 V (yellow) and 4.2 V (green). The fitting plots were obtained by the simulation using the equivalent circuit in (b). (c) Charge transfer resistance (R2) as a function of potential, in which the light blue and green plots were obtained respectively during discharge or charge process. Each resistance was normalized by the R2 value at 2.2 V. Copyright © 2018 Wiley‐VCH Verlag GmbH & Co. KGaA, Weinheim.

The ion diffusion behavior of NiDI during the electrochemical reactions were researched by electrochemical impedance spectroscopy (EIS). Figure 2.2.9 shows the Nyquist plots obtained at different potentials. The electrodes at those potentials were prepared by successive application of constant current at 50 mA/g and relaxation rest for 30 min until the targeted potentials were reached. At all potentials, the Nyquist plots exhibited the semicircles, Warburg and linear regions which were the typical features of Faradaic reactions. The experimental plots were then reproduced by the simulation using the equivalent circuit. Here R1 and R2 are the electrolyte resistance and charge transfer resistance at the surface/bulk interface, CPE1 and CPE2 correspond to the constant phase elements representing the surface/bulk interface and inner-bulk capacitance, and W is the Warburg element for ion diffusion in the bulk. The simulated plots matched well with the experimental data, validating the proposed equivalent circuit model. When the charge-transfer resistance (R2) was plotted versus potential, it showed the potential-dependent trend; the more negative the potential was, the higher value the resistance showed. This trend was contrary to my prediction based on the size difference between PF_6^- and Li^+ ions. At the positive potentials, the redox reactions occur with insertion/de-

sertion of PF_6^- ions, where the diffusion of such large ion should have larger resistance, compared with smaller Li^+ ion diffusion. This unexpected behavior could be explained by the change of the electronic conductivity of NiDI by redox state transitions. In the previous works of our group, the other types of coordination nanosheets were found to undergo decrease of their electronic conductivity by chemical reduction.[11] The behavior observed in this thesis was possibly correlated to the redox-state dependent conductivity as well, which is described in detail in Section 2.5.

As further study of the solid-state ion diffusion of the counter ions, the Warburg region in the Nyquist plot was analyzed to calculate diffusion coefficients (D) of the ions in NiDI. The D values were calculated using the following equations:[10]

$$D = l^2/\tau$$

$$\tau = 2(A_w \cdot C_{int})^2$$

$$A_w = \Delta Z_{re}/\Delta\omega^{-1/2}$$

where l is the characteristic diffusion length (average radius of NiDI particles), τ is the diffusion time, C_{int} is the differential intercalation capacitance and A_w is the Warburg slope. The characteristic diffusion length was 120 nm that was obtained by field emission scanning electron microscopy (FE-SEM) observation of NiDI electrodes (Figure 2.2.10a). The A_w and C_{int} were obtained respectively from the impedance spectra of the Warburg region and the anodic current in the CV at 0.1 mV/s. The diffusion coefficient showed two minimal values at 2.3 V and 3.3 V, where the electrochemical reactions with Li^+ and PF_6^- insertion/desertion occurred, respectively (Figure 2.2.10b). The D values at those potentials were close to or slightly larger than those of representative layered compounds such as $LiCoO_2$ or graphite.[10,12]

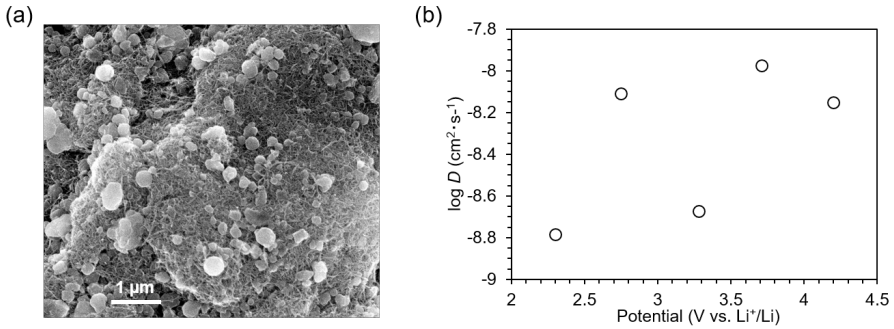

Figure 2.2.10. (a) FE-SEM image of the NiDI electrode. NiDI were observed as white particles that were surrounded by MWCNT having fiber-like morphology. (b) The diffusion coefficient of NiDI at various potentials.

2.2.3 Energy storage function as a cathode material

NiDI, a material showing the unique electrochemical property of multielectron transfer with anion/cation insertion, was then investigated as a cathode material in a lithium-based rechargeable battery to investigate its energy storage functions. Charge-discharge tests at several current densities were firstly carried out to reveal specific capacity of NiDI. The potential window was set to 2.0 ~ 4.5 V to include the redox reactions with two kinds of counterion insertion/desertion. The obtained curves at different current densities indicated large dependence of the current density to the capacity of NiDI, and two plateaus were observed in all the curves (Figure 2.2.11a). These plateaus correspond to the reactions with Li^+/PF_6^- insertion/desertion as observed in the CVs in Figure 2.2.7c. The maximum specific capacity of 155 mAh/g was achieved on the discharge curve at 10 mA/g. Cycle performance was investigated by repeating charge-discharge cycles at 250 mA/g (Figure 2.2.11b). The result showed that the NiDI electrode retained about 80% of the initial capacity, and the coulomb efficiency was mostly higher than 99%. In the initial 50 cycles, the capacity of NiDI increased up to 121% followed by gradual decay, which is considered to be an activation process (exposure of the surface to the electrolyte) or formation of solid-liquid interface (SEI) by decomposition of the electrolyte. This process also caused relatively low coulomb efficiency in those cycle numbers. Through the above measurements, NiDI was found to possess excellent energy storage properties; it marked quite high specific capacity and good cyclability as a MOF-based cathode material (Table 2.2.1),[13] and the capacity was comparable to commercially used cathode materials in lithium ion batteries such as $LiCoO_2$ or $LiFePO_4$.[14]

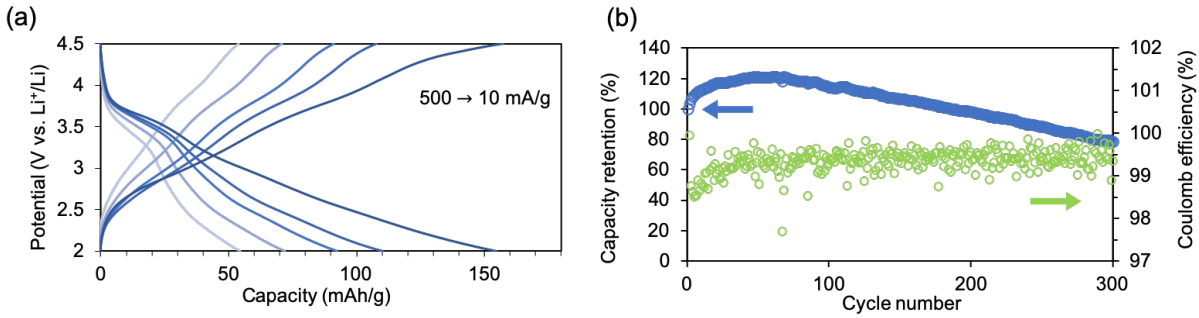

Figure 2.2.11. (a) Charge-discharge curves of NiDI at current densities of 10 ~ 500 mA/g. (b) Capacity retention and coulomb efficiency of NiDI for 300 cycles, being measured at 250 mA/g. Copyright © 2018 Wiley‐VCH Verlag GmbH & Co. KGaA, Weinheim.

Table 2.2.1. Energy storage performances of the representative MOF-based cathode materials tested in lithium-based rechargeable batteries. Copyright © 2018 Wiley‐VCH Verlag GmbH & Co. KGaA, Weinheim.

Cathode material	Specific capacity (mAh/g)	Rate	Potential window (V vs. Li^+/Li)	Tested cycle number	Reference
NiDI (This work)	**155**	**10 mA/g**	**2.0 - 4.5**	**300**	**-**
MIL-53	75	0.025 C	1.5 - 3.5	50	13a
MIL-132	50	10 C	2.3 - 3.75	-	13b
$Rb_{0.7}Mn_{1.15}[Fe(CN)_6]\cdot 2.5H_2O$	< 60	50 mA/g	2.0 - 4.3	100	13c
$K_{2.5}[(VO)_2(HPO_4)_{1.5}(PO_4)_{0.5}(C_2O_4)]$	66	40 mA/g	2.5 - 4.6	60	13d
$K_2Mn[Mn(CN)_6]$	197	30 mA/g	2.0 - 4.2	10	13e

The high specific capacity of NiDI was achieved by the redox reactions based on multielectron transfer with Li^+/PF_6^- transport, in which the contribution of each reaction to the whole capacity was hard to estimate from the above charge-discharge curves. Thus, the CVs in different potential windows (Figure 2.2.7c) were further analyzed to breakdown the specific capacity profile. The capacities calculated from those CVs indicated that the redox state transition of NiDI between non-charged and reduced states with Li^+ transport has higher contribution to the other PF_6^--related reaction. This is possibly due to limitation of the space in NiDI for accommodating larger PF_6^- ions, compared with the case of Li^+ ions.

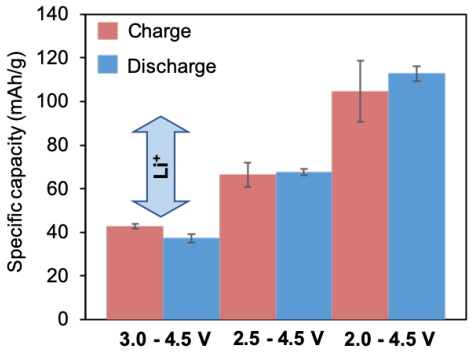

Figure 2.2.12. (a) Charge-discharge curves of NiDI at current densities of 10 ~ 500 mA/g. (b) Capacity retention and coulomb efficiency of NiDI for 300 cycles, being measured at 250 mA/g. Copyright © 2018 Wiley‐VCH Verlag GmbH & Co. KGaA, Weinheim.

2.2.4 Mechanisms of the electrochemical behavior

The crystal structures of oxidized (charged) and reduced (discharged) states were examined by *ex situ* PXRD measurements of the respectively charged materials. The charged samples were prepared by applying constant potential (2.0 and 4.2 V) for 3 days, being followed by washing process with acetonitrile under an argon atmosphere. The diffraction patterns were displayed in Figure 2.2.13, in which the patterns of the respectively charged samples were almost identical to the pattern of pristine NiDI, confirming that the samples were not decomposed at the electrochemical processes. Additionally, the results indicate that the lattice expansion along intralayer and interlayer did not occur even after the insertion of the counterions. Therefore, the ion-insertion process was possibly unlike typical layered compounds such as graphite: the counterions were inserted through the pores and accommodated in the space (Figure 2.2.13b), or the interlayer distance did not change even the ions exist between the layers. The integrity of the electrochemically stable framework was further confirmed by IR and Raman spectroscopies of oxidized/reduced NiDIs, in which they did not show obvious difference from the pristine sample (Figure 2.2.13c,d).

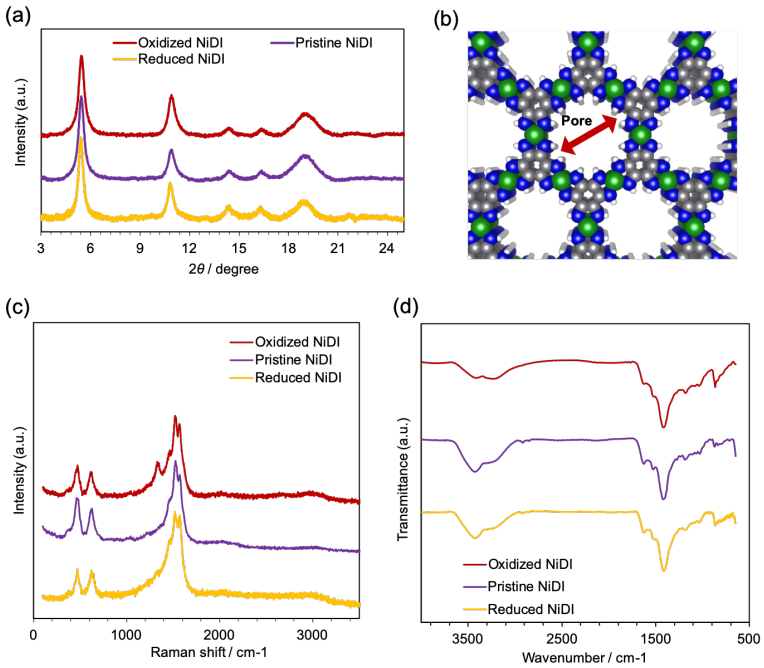

Figure 2.2.13. (a) PXRD patterns of the oxidized, pristine and reduced NiDIs. (b) Schematic image of the porous structure of NiDI (C: gray, N: blue, H: white, Ni: green). (c) Raman and (d) IR spectra of the respectively charged NiDIs. Copyright © 2018 Wiley‐VCH Verlag GmbH & Co. KGaA, Weinheim.

From the viewpoint of electronic structures, the mechanism of the electrochemical behavior of NiDI was researched using DFT calculations.[15] Figure 2.2.14 shows the electronic band structure of NiDI with AA stacking model after structure relaxation. As reported in the literatures, NiDI did not have a band gap around the Fermi level, suggesting electronically metallic conductivity. This metallic nature was also confirmed by projected density of states (PDOS) of NiDI, which showed non-zero electronic states at the Fermi level. PDOS gives information about not only the conductivity but also the redox reactions of the material, because oxidation/reduction reactions are essentially extraction/injection of electrons from/to the electronic states. The PDOS of NiDI was then compared with the experimental dQ/dV curve which was obtained by converting the discharge curve at 10 mA/g in Figure 2.2.11a. As a result, the PDOS was found to well-represent the feature of the dQ/dV curve especially around the Fermi level, validating discussion of the electrochemical behavior with the theoretical calculations. In the PDOS, the states of Ni, C and N atoms are crossing the Fermi level, and thus both the metal center and the ligand were involved as the redox centers during the electrochemical reactions.

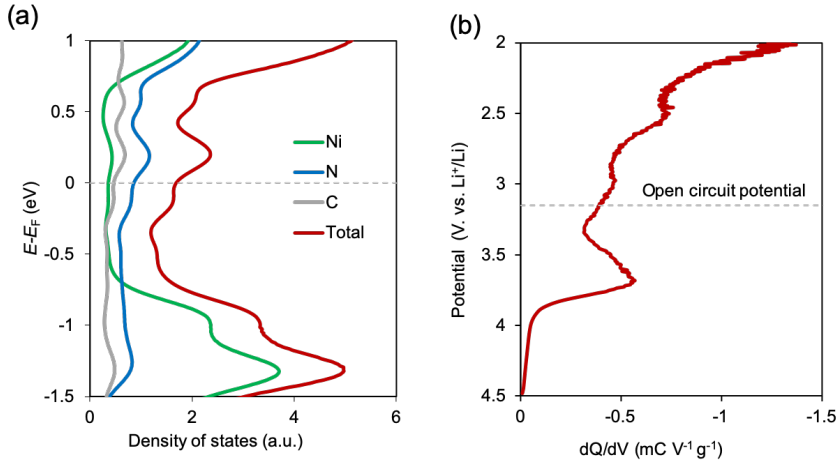

Figure 2.2.14. (a) Theoretically calculated PDOS and (b) the experimentally obtained dQ/dV curve of NiDI.

The electronic states of each atom was also studied by *ex situ* XPS of the respectively charged NiDIs. In N 1s region (Figure 2.2.15), the spectra of NiDI at 3.2 V and 2.0 V were fitted with three or four peaks (398.3, 399.3 and 400.5 eV) respectively as described in Section 2.2.1. Figure 2.2.15b represents the partial chemical structures of NiDI with the colored circles, the colors of which correspond to deconvoluted peaks in Figure 2.2.15a.

When NiDI was oxidized from 3.2 V to 4.2 V, the relative peak area of imine group (-

C=NH-Ni) increased, which indicates oxidation of the ligand. The blue peak also became more intense and broader, which was caused by the partial decomposition of NiDI with Ni removal, or oxidation of non-coordinating N-containing groups. Additionally, unstable radical cationic groups (-NH^{2+}) may have been formed (green peak at 402.3 eV) when they were highly oxidized.

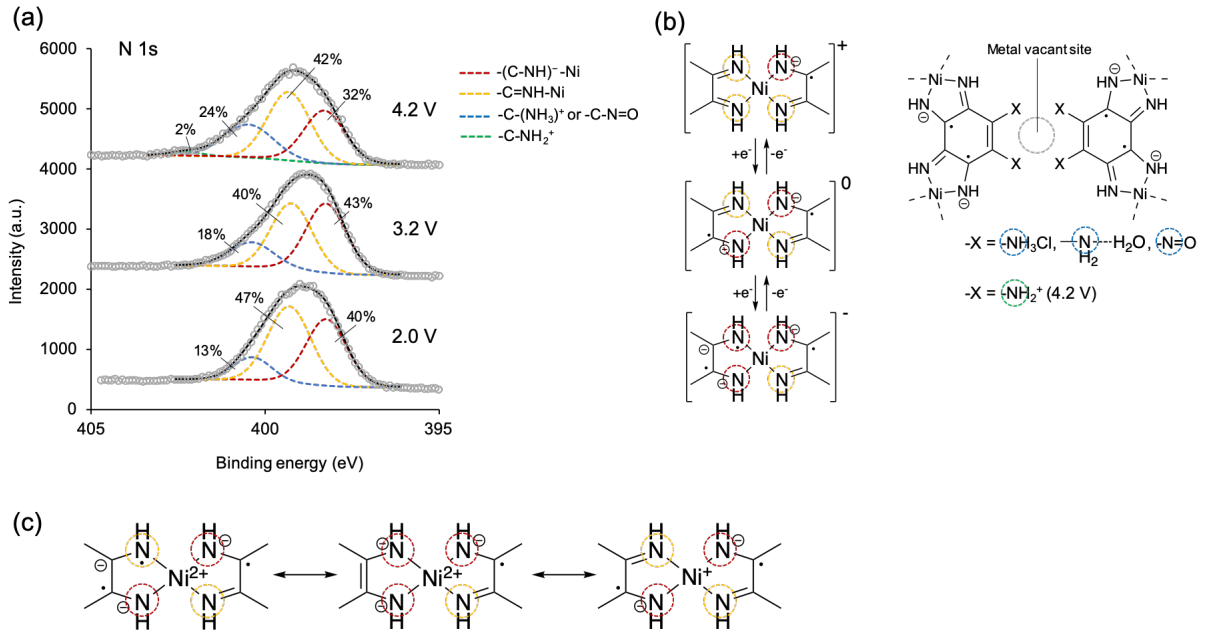

Figure 2.2.15. (a) N 1s region of the X-ray photoelectron spectra of the oxidized, non-charged and reduced NiDIs. The oxidized and reduced NiDIs were prepared by applying the potentials of 4.2 V and 2.0 V, respectively. The inset percentage ratios represent the relative content (area) ratios of each species. The colors of the peaks correspond to the colors of the dashed circles on the respective N atoms in (b). (c) The resonance structures of the Ni-centered complex units in reduced NiDI.

On the other hand, the peak at higher BE (yellow) increased by reduction reaction, unlike typical behavior of reduced materials. Then, the resonance structures of the Ni centered motif (Figure 2.2.15c) were considered to rationalize this trend. In the negatively charged motif, there are mainly three resonance structures. In the left structure, the negative charge is localized on a carbon atom, and the neighboring nitrogen (yellow) should show higher BE than the -NH^--group. In addition, the sp^2 character of the C-N bond may be weakened, which also increases BE. Therefore, this structure can reasonably explain the experimental result. On the other hand, in the middle structure, the injected negative charge is localized on the amine groups, suggesting

peak shift to lower BE. Finally, mono-valent Ni is usually unstable, so the right structure can be excluded from the possible model. Based on these considerations, we can conclude that the left structure is the most reasonable model for the reduced NiDI.

Figure 2.2.16 shows the C 1s spectra of NiDIs. The peak at 285.7 eV (yellow) correspond to -(C-NH)$^-$-Ni or -C-X, and the peak at 286.9 eV (green) represents –C=NH-Ni in NiDI. The red peaks at 284.8 eV and the blue beaks at 288.3 eV were derived from contamination of the surface (adventitious carbon), in which the latter may also include SEI carbon.[16] Only the spectrum at 4.2 V had another peak at 290.3 eV that could be assigned to highly oxidized carbon in SEI. At 3.2 V, the relative ratio of the carbon species of NiDI (yellow and green) were almost equal. Then, after oxidizing NiDI, the peak intensity at higher BE (green) increased, while reduced NiDI showed its decrease. These trends are qualitatively in good agreement with the N 1s spectra.

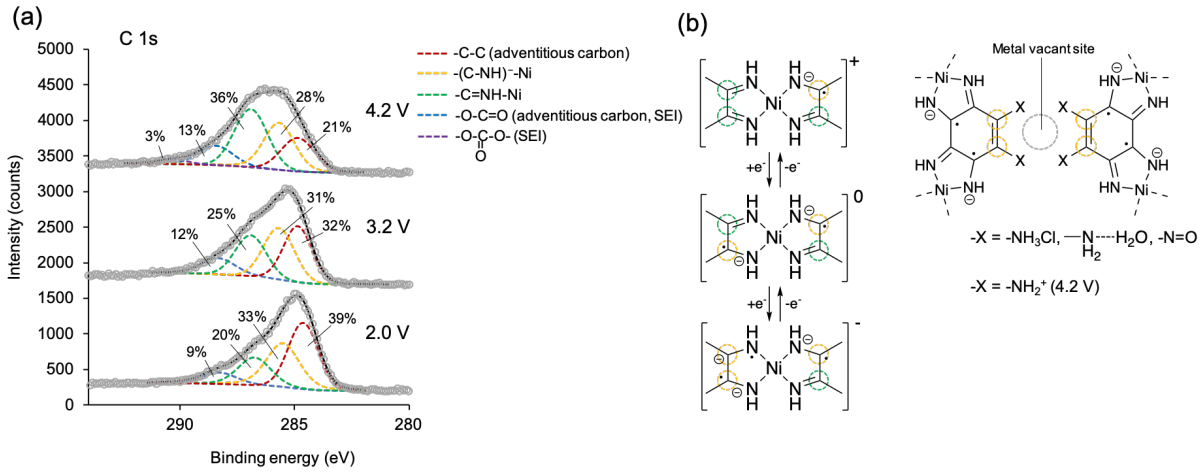

Figure 2.2.16. (a) C 1s region of the X-ray photoelectron spectra of the oxidized, non-charged and reduced NiDIs. The inset percentage ratios represent the relative content (area) ratios of each species. The colors of the peaks correspond to the colors of the dashed circles on the respective C atoms in (b).

The Ni 2p3/2 spectra were fitted with three or four peaks (Figure 2.2.17a). The Ni 2p3/2 peaks (red, 855.1 eV and yellow, 856.0 eV) were derived from Ni atoms in NiDI (Figure 2.2.17b). The green broad peaks are F *KLL* auger peaks from electrolyte residue (PF_6^-) or SEI.[17] Finally, the blue broad peaks are the satellites of Ni 3d to 4p transition. At 3.2 V, Ni ion were basically divalent states, as indicated by absence of an intense satellite peak near 860 eV that

appears when Ni has unpaired electrons.[7] Therefore, the Ni atom had low-spin d^8 electrons that is typical for square planar nickel complexes. The red and yellow peaks were possibly originated from Ni(II) ions surrounded by the ligands with different oxidation states, respectively; the higher BE of the yellow peak would be due to partial oxidation of the ligand. After oxidization or reduction of NiDI, the relative ratio of red and yellow peaks changed without further peak splitting. Therefore, the divalent state of Ni ions were considered to be retained at each potential.

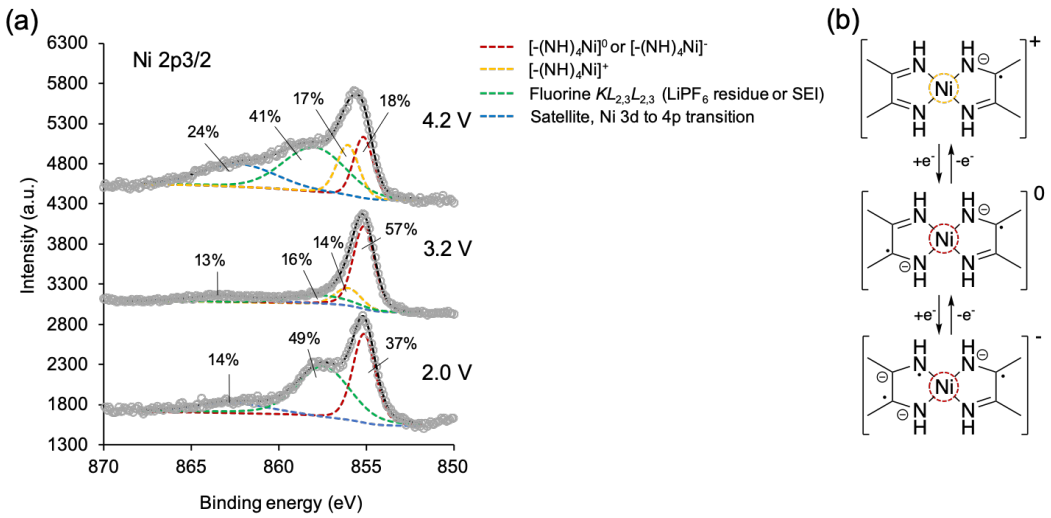

Figure 2.2.17. (a) Ni 2p3/2 region of the X-ray photoelectron spectra of the oxidized, non-charged and reduced NiDIs. The inset percentage ratios represent the relative content (area) ratios of each species. The colors of the peaks correspond to the colors of the dashed circles on the respective Ni atoms in (b).

2.3.5 Redox state-dependent electronic conductivity of NiDI

In the previous studies of the electronically conductive coordination nanosheets, some of the materials were found to change their electronic conductivity depending of their redox states.[11] For instance, NiDT, the nanosheet synthesized from a nickel(II) ion and benzenehexathiol, increased its conductivity by several magnitude of orders by chemical oxidation of its motifs.[11b] Given those studies, NiDI may have a potential to exhibit redox state-dependent conductivity. The EIS measurements in Section 2.2.2 in fact suggested the possibility of conductivity change at different electrochemical potentials. The conductivity of NiDI was then investigated using organic electrochemical transistors. Figure 2.2.18a shows the schematic image of the device configuration, in which the NiDI film was placed on the gold wire-patterned substrate. As an electrolyte, $LiPF_6$ saturated ionic liquid, 1-butyl-3-methylimidazolium bis(trifluoromethylsulfonyl)imide (BMIM•TFSI), was used. $LiPF_6$ salt was added to ensure insertion/desertion of ions because the sizes of the cation and anion of BMIM•TFSI were relatively large, which may cause difficulty in insertion into the NiDI framework.

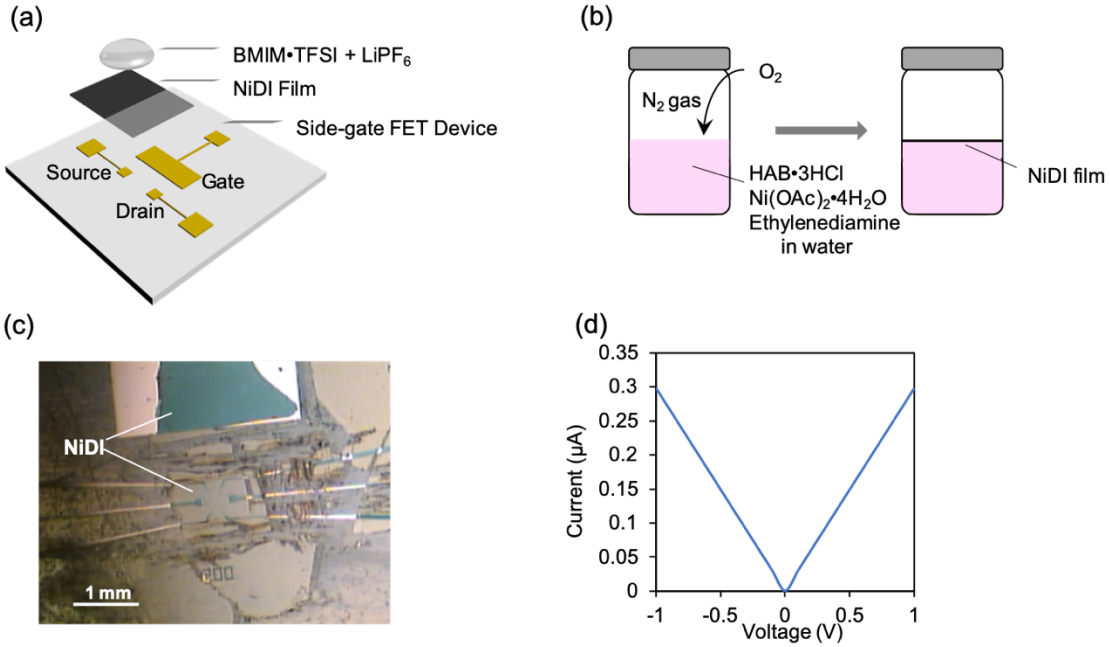

Figure 2.2.18. (a) Schematic illustration of the device configuration of the organic electrochemical transistor. (b) The schematic image of the synthesis method of a NiDI film. (c) The optical spectroscopic image of the NiDI film on the side-gate FET device. The films around the measurement active area was patterned by hand-scratching. (d) The output curve of NiDI that was obtained from the current between the source and drain electrodes in the device shown in (c).

Firstly, the NiDI film was synthesized[1c] and transferred on to the substrate as illustrated in Figure 2.2.18b. The appearance of the film was quite uniform under optical microscopy observation (Figure 2.2.18c), and the average thickness was about 100 nm. The electronic conductivity of the device was measured before addition of the electrolyte, finding that the film showed ohmic behavior (Figure 2.2.18d). The conductivity was calculated to be 3.0×10^{-2} S/cm, which is comparable to the value in the previous study of our group.[1d]

After confirmation of successful transfer of the NiDI film, $LiPF_6$-saturated BMIM•TFSI was added on the active measurement area of the device under a nitrogen atmosphere. However, after a while, NiDI absorbed the electrolyte, swelled, formed winkles, and caused electric disconnection between the film and the gold electrodes (Figure 2.2.19a). Therefore, the source and drain electrode areas were protected by pasting the inert polymer (CYTOP®) on the NiDI film (Figure 2.2.19b).

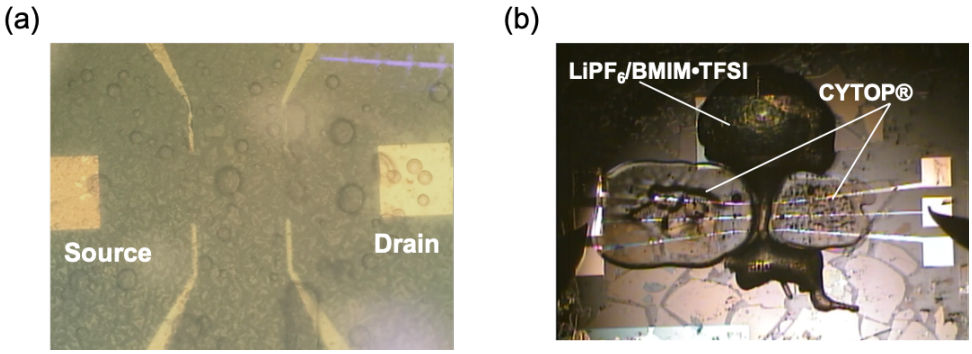

Figure 2.2.19. Optical microscopic images of (a) the organic electrochemical transistor device after addition of $LiPF_6$/BMIM•TFSI and (b) the device with CYTOP® for protection of the source and drain electrodes. In (a) the NiDI film absorbed the electrolyte and formed small wrinkles on the entire area, which is seen as the pattern in the image.

When the electronic conductivity measurements on different gate voltages were carried out by the typical method (applying each voltage for relatively short time), the output current included large contribution of ion transport in the ionic liquid layer. Then, in order to evaluate the current originated only from electron transport in the film, the stress measurement method was employed. In this method, each voltage was kept constant for 15 min, in which current derived from the ion transport decayed as a function of time while that from the electron transport was constant (Figure 2.2.20a). Therefore, at the end of the measurement time, the

current should include the contribution mostly from the electron transport. Moreover, the potentials on the gate and drain electrodes were fixed to be equal while the source electrode was grounded, so that the gate current leakage could be removed from the drain current. Thus, the drain current was used to evaluate the electronic conductivity of NiDI (Figure 2.2.20b).

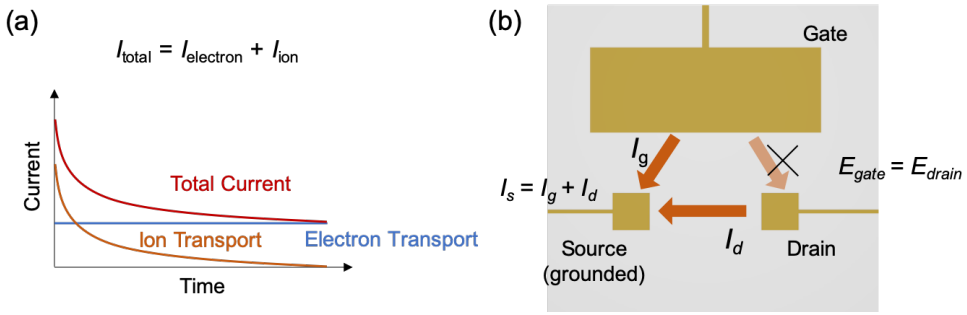

Figure 2.1.1. Schematic image of the stress measurement method representing (a) current behavior depending on measurement time, and (b) potentials and expected current flows on the device.

Figure 2.2.21a represents the accumulated charge on the NiDI film at respective gate voltages, which was calculated by time-integration of the gate current. When the gate voltage was positively scanned, the NiDI showed the reduction reaction as indicated by the downwardly convex peak at 1 V. The film became the non-charged state again at 0 V, being followed by the redox state transition between the non-charged and oxidized states in the positive voltage region, where the quasi-reversible peaks were observed. These results suggest that the redox states of the NiDI film were successively controlled on the device. The current intensity on each electrode at different voltages were then obtained by extracting the current intensity at the last points of the stress curves (at t = 15 min, t is a measurement time). In Figure 2.2.21b, the source and drain current intensities were enough higher than the gate current intensity, suggesting that the contribution of ion transport was negligible. Because these plots were obtained at several source-drain voltages (that was equal to gate voltages), the respective current intensities were divided by the corresponding voltages to calculate conductance of the film. The resulting plots in Figure 2.2.21c clearly indicate the correlation between conductance and gate voltage; conductance of NiDI decreased by the reduction reaction while it increased by the oxidation reaction. The flat regions possibly represent the hysteresis of the electrochemical reactions. The mechanism of this conductivity change would be related to increase of positive carriers in NiDI

by the oxidation reaction. However, the carrier type of NiDI has not been revealed yet, and understanding of the mechanism requires further investigation.

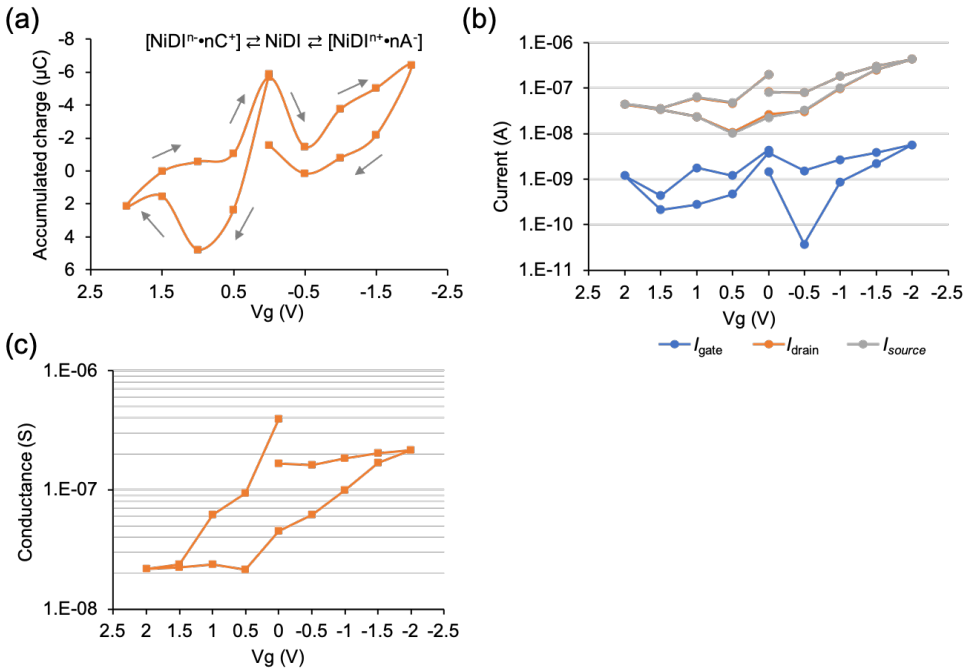

Figure 2.2.21. (a) Accumulated charge on the NiDI film at respective potentials. C and A in the reaction formula represent a cation and an anion in the electrolyte. (b) Current detected at each electrode at different potentials. (c) Conductance of the NiDI film which was calculated from I_{drain} in (b).

2.3 Experimental section

2.3.1 General

(a) Reagents

All the organic solvents were purchased from commercial sources and used without further purification. Water for synthesis was purified with AUTOPURE WD500 (Yamato Scientific Co., Ltd.). Hexaaminobenzene trihydrochloride (HAB•3HCl) and NiDI were synthesized following the literatures.[1b,20] 1,3,5-Trichlorobenzene, 30% fuming sulfuric acid, potassium nitrate, ammonia gas, 10% palladium on carbon, ammonia gas, hydrochloric acid, nickel acetate tetrahydrate, 32% ammonia aqueous solution, multi-walled carbon nanotube, polyvinylidene difluoride, 1M lithium hexafluorophosphate in ethylene carbonate/diethyl carbonate (3:7), bis(trifluoromethylsulfonyl)imide, lithium hexafluorophosphate and CYTOP® were purchased from commercial sources.

(b) Machine specifications

NMR spectra were measured with a Bruker DRX-500 spectrometer. Tetramethylsilane ($\delta = 0.00$) was used as an internal standard for ^{1}H NMR spectra, and $CDCl_3$ ($\delta = 77.0$) was used as an internal standard for ^{13}C NMR spectra. The HR-TEM observation was conducted by a JEM-ARM200F (JEOL) was used. The FT-SEM observation was carried out using a JSM-7400 FNT (JEOL). The PXRD patterns were obtained using synchrotron radiation ($\lambda = 1.08$ Å) at Beamline BL44B2, Super Photon ring-8 GeV (SPring-8, Japan). The X-ray photoelectron spectroscopy measurements were conducted using PHI 5000 Versa Probe (ULVAC-PHI Inc.) with Al Kα (15 kV, 25W) as the X-ray source. The Raman spectra were measured by LabRAM HR Evolution (HORIBA Scientific). The Fourier transform infrared (FTIR) spectra were obtained by a KBr pellet method using Nicolet iS50 FT-IR (Thermo Fisher Scientific). The electrochemical measurements were carried out with multichannel potentio/galvanostat VMP-3 (Bio-Logic Scientific Instruments), HJ1001 SD8 (Hokuto Denko Co.), ALS 650 DT electrochemical analyzer (ALS Co., Ltd.) and HOKUTO HZ-3000 (Hokuto Denko Co.).

(c) Computational methods

The density functional theory (DFT) calculations were conducted using the package, QUANTUM ESPRESSO[15] and Gaussian09 revision E.01 program.[19] For the initial calculation model of NiDI, the mono-nuclear [Ni-N_4] complex was submitted to structure optimization

using Gaussian09 revision E.01 program with a basis set of B3LYP/6-31G(d). The optimized structure was then appropriately trimmed and tiled to make a unit cell of NiDI. The structure of the tiled NiDI model was further relaxed using QUANTUM ESPRESSO. In the calculation of QUANTUM ESPRESSO, the projected augmented wave method with Perdew-Burke-Ernzerhof (PBE) exchange-correlation functional was employed. The self-consistent calculation and electronic band structure calculation of NiDI were carried out with a kinetic energy cutoff of 408 eV and at a Γ-contained 6 × 6 × 6 **k**-point mesh. The projected density of states of NiDI were calculated at a Γ-contained 12 × 12 × 12 **k**-point mesh.

2.3.2 Synthesis

(a) Synthesis procedure of 1,3,5-trichloro-2,4,6-trinitrobenzene.

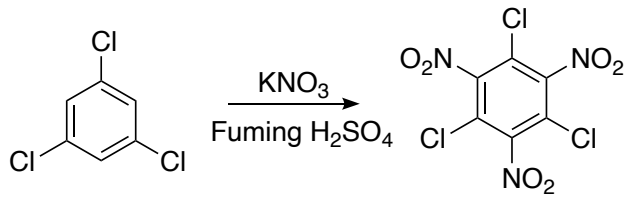

1,3,5-Trichloro-2,4,6-trinitrobenzene was synthesized from 1,3,5-trichlorobenzene following the literature.[20] To 30% fuming sulfuric acid (125 mL) potassium nitrate (22.6 g, 0.224 mol) was added batch by batch and the solution was stirred at 80°C until all potassium nitrate was dissolved. 1,3,4-Trichlorobenzene (10.2 g, 0.0562 mol) was then added little by little to the solution, and it was stirred at 110°C for 4 h. The solution was cooled to room temperature and carefully poured into ice. The precipitation was collected by filtration, being followed by successive wash with mass water. After drying the solid, it was further purified by flash column chromatography on silica gel (eluent: ethyl acetate/*n*-hexane = 1/9) to obtain the product as a while solid (14.6 g, 0.0461 mol) in 82% yield.

1,3,5-Trichloro-2,4,6-trinitrobenzene: Isolated yield: 82%. White solid.

(b) Synthesis procedure of 1,3,5-triamino-2,4,6-trinitrobenzene.

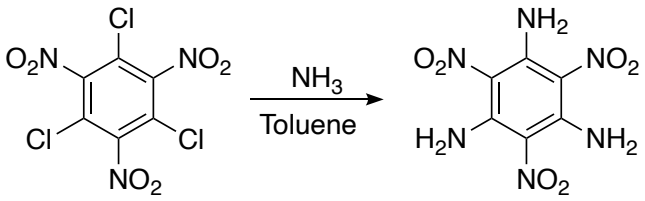

1,3,5-Triamino-2,4,6-trinitrobenzene was prepared from 1,3,5-trichloro-2,4,6-trinitrobenzene following the literature.[20] 1,3,5-Trichloro-2,4,6-trinitrobenzene (0.600 g, 1.90 mmol) was added to toluene (14 mL), and ammonia gas was vigorously bubbled through the solution. The solution was stirred at 110°C for overnight with continuous gas bubbling. The precipitation was then collected by filtration, washed with water and dried under vacuum to obtain the product as a yellow solid (154.4 mg, 0.598 mol) in 31.5% yield. The product was directly used in the next step to synthesize hexaaminobenzene trihydrochloride without further characterization due to its explosive property.

1,3,5-Triamino-2,4,6-trinitrobenzene: Isolated yield 31.5%. Yellow solid.

(c) Synthesis procedure of hexaaminobenzene trihydrochloride (HAB•3HCl).

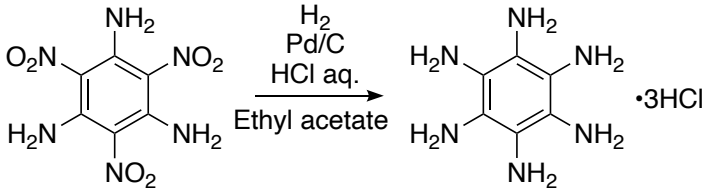

Hexaaminobenzene trihydrochloride was synthesized from 1,3,5-triamino-2,4,6-trinitrobenzene following the literature.[20] In the vessel, 1,3,5-triamino-2,4,6-trinitrobenzene (360 mg, 1.39 mmol) and 10% palladium on carbon (75 mg) was placed, 40 mL of ethyl acetate was added, and the atmosphere was exchanged with hydrogen gas. The solution was vigorously stirred at 40°C under an 1 atm hydrogen atmosphere for 3 days. 32% hydrochloric acid (11 mL) was then added and further stirred for 3h. The precipitation was collected by filtration under inert gas, and the product was extracted with water. The product-containing solution was again dropped into concentrated hydrochloric acid to recrystallize it. The precipitation was again collected by filtration and dried under vacuum to obtain the product as a pale red color solid (201 mg, 0.726 mmol) in 52.2 % yield.

Hexaaminobenzene trihydrochloride (HAB•3HCl): Isolated yield 45%. Pale red solid. Elemental analysis Calcd (%) for $C_6H_{15}N_6Cl_3$: C 25.96, H 5.45, N 38.31, Cl 30.28. Found: C 26.31, H 5.72, N 37.98, Cl 29.79.

(d) Synthesis procedure of powder-state NiDI.

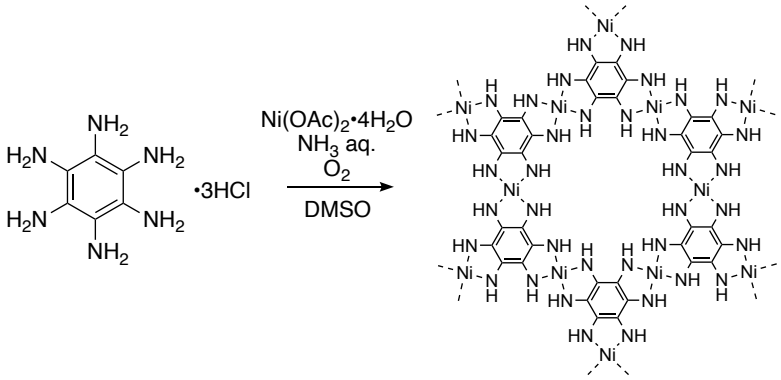

Powder-state NiDI was synthesized from hexaaminobenzene trihydrochloride by the modified procedure based on the literature.[1b] Under an argon atmosphere, HAB•3HCl (20 mg, 0.072 mmol) and nickel acetate tetrahydrate (27 mg, 0.11 mmol) were placed in a 20 ml vial, and dissolved in 6ml of dimethyl sulfoxide degassed with nitrogen gas. To the solution, 32% ammonia aqueous solution (0.8 g) was added and the solution was exposed to air after tightly closing the cap. The cap was then slightly opened and the reaction solution was placed at 60°C for 12 h. The precipitation was collected by centrifuge, washed with water and acetone, and dried at 120°C under vacuum to obtain the product as a black powder.

(e) Synthesis procedure of film-state NiDI.

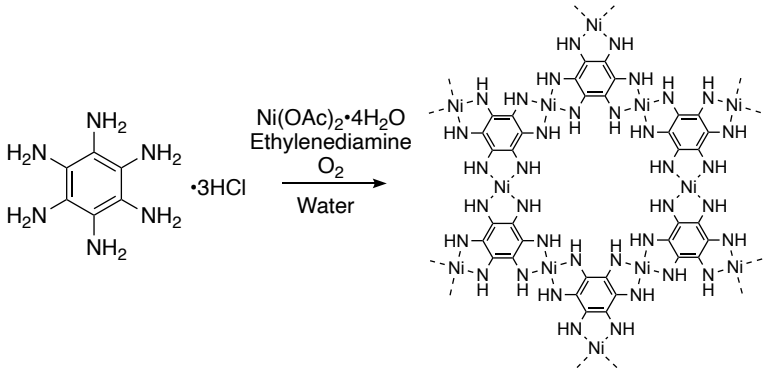

Film-state NiDI was synthesized by the modified procedure based on the literature.[1c] Under an argon atmosphere, HAB•3HCl (1.1 mg, 0.0039 mmol) and nickel acetate tetrahydrate (1.9 mg, 0.0077 mmol) were placed in a 60 ml vial, and dissolved in 2.3 ml of water degassed with nitrogen gas. To the solution, ethylenediamine (2.3 μL, 0.034 mmol) was added and a cap of the vial was tightly closed. The vial was then exposed to air and left for 12 h at room temperature. The black film was formed on the surface of the solution, which was transferred onto a substrate by scooping. After drying the film, it was immersed in water and acetone to remove residues.

2.3.3 Fabrication of the NiDI electrodes and the batteries.

(a) Preparation of the NiDI-containing electrodes

The NiDI electrodes for the electrochemical measurements were fabricated from NiDI, multi-walled carbon nanotube (MWCNT) and polyvinylidene difluoride (PVdF) by a typical electrode preparation method for electrodes in lithium ion batteries. NiDI, MWCNT and PVdF were firstly mixed with the ratio of 7:2:1 (based on non-volatile weight). The mixture was then grinded with motor with gradual addition of *N*-methylpyrrolidone until it becomes a slurry state. The slurry was then pasted onto aluminum foil and dried at 110°C under vacuum. The electrode was then cut out to fit it in a battery cell. The loading amount of NiDI on the electrode was ~ 2mg/cm^2.

(b) Preparation of the lithium batteries.

For the preparation, coin-type aluminum cells or assembly type SUS cells were used. The NiDI-containing electrode was firstly immersed in 1 M $LiPF_6$ in mixture of ethylene carbonate and diethyl carbonate for a while. The electrode was then placed as a cathode in a cell, and covered with TORAYCA® TGP-H-60 (Toray Industries, Inc.) to ensure the electrical connection of the NiDI-containing electrode. After addition of several drops of the electrolyte, a polymer-based separator was put, followed by further addition of the electrolyte and a lithium metal on top.

2.3.4 Sample preparations for the respective characterizations.

(a) Samples for HR-TEM observation

Little amount of NiDI powder was added to ethanol and subjected to ultrasonication for several hours to disperse the NiDI particles. Large particles were removed by centrifuge and the top solution was drop casted onto a copper grid coated with supporting polymers. The grid was dried at 110°C under vacuum to insert into the microscope.

(b) Samples for the ex situ spectroscopic measurements of oxidized and reduced NiDIs

The samples for the ex situ IR and Raman spectroscopic measurements were prepared by applying constant potentials on the NiDI-containing electrodes in lithium batteries (2.0 V and 4.2 V for reduced and oxidized NiDIs, respectively). After completion of the electrochemical reactions, the battery cells were dissembled under inert atmosphere, and the electrodes were successively washed with acetonitrile to remove the electrolyte. The electrodes were dried under vacuum at room temperature. For Raman spectroscopic measurements, the electrodes were directly used without further process. For IR spectroscopic measurements, the electroactive parts containing NiDI were collected by scratching the electrodes and mixed with potassium bromide (KBr) to make pellets.

(c) Samples for the ex situ PXRD and XRD measurements of oxidized and reduced NiDIs

In order to remove diffraction signals of MWCNT and PVdF, the respectively charged NiDIs were prepared by using pure NiDI pellets instead of the fabricated electrodes. Except for the contents of the electrode, the preparation method was the same method as the IR and Raman spectroscopic measurements. For XPS measurements, the dried samples were directly used without further process. Additionally, non-charged NiDI was also placed in a lithium battery cell without applying any potential for comparison with the other samples. For XRD measurements, the dried pellets were grinded to obtain powder samples, which was packed into glass capillaries and sealed under an argon atmosphere.

2.3.5 X-ray photoelectron spectra of the charged NiDIs.

The parameters used for fitting to reproduce the respective spectra were listed below.

(a) Oxidized NiDI

Table 2.3.1. Fitting parameters for the spectrum of oxidized NiDI in N 1s region.

Species	Area	Position (eV)	Height (counts)	FWHM
-(C-NH)$^-$-Ni	1343	398.30	868	1.39
-C=NH-Ni	1742	399.32	1133	1.45
-C-$(NH_3)^+$ or -C-N=O	976	400.48	543	1.69
-C-NH_2^+	87	402.29	66	1.14

Table 2.3.2. Fitting parameters for the spectrum of oxidized NiDI in C 1s region.

Species	Area	Position (eV)	Height (counts)	FWHM
C-C (adventitious carbon)	860	284.85	471	1.72
-(C-NH)$^-$-Ni	1161	285.67	663	1.57
-C=NH-Ni	1475	286.90	815	1.70
-O-C=O (adventi-tious carbon)	538	288.43	272	1.77
-O-C(=O)-O- (SEI)	105	290.29	63	1.48

Table 2.3.3. Fitting parameters for the spectrum of oxidized NiDI in Ni 2p3/2 region.

Species	Area	Position (eV)	Height (counts)	FWHM
$[-(NH)_4Ni]^0$ or $[-(NH_4)Ni]^-$	1125	855.15	759	1.33
$[-(NH_4)Ni]^+$	1100	856.04	629	1.50
Fluorine $KL_{2,3}L_{2,3}$ ($LiPF_6$ or SEI)	2565	857.96	550	4.18
Satellite (Ni 3d to 4p transition)	1536	862.25	277	4.98

(b) Non-charged NiDI

Table 2.3.4. Fitting parameters for the spectrum of non-charged NiDI in N 1s region.

Species	Area	Position (eV)	Height (counts)	FWHM
$-(C-NH)^-$-Ni	1772	398.25	1166	1.36
-C=NH-Ni	1642	399.24	1104	1.40
$-C-(NH_3)^+$ or -C-N=O	726	400.38	418	1.50

Table 2.3.5. Fitting parameters for the spectrum of non-charged NiDI in C 1s region.

Species	Area	Position (eV)	Height (counts)	FWHM
C-C (adventitious carbon)	1307	284.85	795	1.48
$-(C-NH)^-$-Ni	1250	285.67	734	1.60
-C=NH-Ni	996	286.90	585	1.60
-O-C=O (adventitious carbon)	501	288.32	232	1.77

Table 2.3.6. Fitting parameters for the spectrum of non-charged NiDI in Ni 2p3/2 region.

Species	Area	Position (eV)	Height (counts)	FWHM
$[\text{-(NH)}_4\text{Ni}]^0$ or $[\text{-(NH}_4\text{)Ni}]^-$	2186	855.12	1286	1.46
$[\text{-(NH}_4\text{)Ni}]^+$	549	856.02	281	1.75
Fluorine $KL_{2,3}L_{2,3}$ ($LiPF_6$ or SEI)	608	857.59	131	4.00
Satellite (Ni 3d to 4p transition)	502	862.02	97	4.65

(b) Reduced NiDI

Table 2.3.7. Fitting parameters for the spectrum of reduced NiDI in N 1s region.

Species	Area	Position (eV)	Height (counts)	FWHM
$\text{-(C-NH)}^-\text{-Ni}$	1411	398.25	923	1.37
-C=NH-Ni	1640	399.32	1063	1.45
$\text{-C-(NH}_3\text{)}^+$ or -C-N=O	437	400.38	321	1.28

Table 2.3.8. Fitting parameters for the spectrum of reduced NiDI in C 1s region.

Species	Area	Position (eV)	Height (counts)	FWHM
C-C (adventitious carbon)	1784	284.62	1091	1.54
$\text{-(C-NH)}^-\text{-Ni}$	1513	285.50	732	1.70
-C=NH-Ni	911	286.75	460	1.70
-O-C=O (adventitious carbon)	412	288.27	191	1.77

Table 2.3.9. Fitting parameters for the spectrum of reduced NiDI in Ni 2p3/2 region.

Species	Area	Position (eV)	Height (counts)	FWHM
$[\text{-}(NH)_4Ni]^0$ or $[\text{-}(NH_4)Ni]^-$	2067	855.13	1110	1.53
Fluorine $KL_{2,3}L_{2,3}$ ($LiPF_6$ or SEI)	2746	857.42	643	3.51
Satellite (Ni 3d to 4p transition)	761	862.59	126	4.97

2.3.6 Device fabrication of the organic electrochemical transistor.

The substrates the side-gate transistor with gold electrodes were prepared by photolithography and vapor deposition methods. A glass substrate was firstly spin coated with positive photoresist, LOR5B, and heated at 80°C for 20 min to dry the resist. The substrate was exposed to intense UV light through a photomask and immersed in to wash out the degraded resist in the gold-patterning area. Titanium was evaporated onto the substrate under presence of air to deposit titanium oxide, being followed by gold vapor deposition. The Substrate was then immersed in *N*-methylpyrrolidone to remove remaining photoresist with unnecessary metals, and the surface was cleaned by ozone plasma etching for 5 min. On the electrode-patterned substrate, a synthesized NiDI film was transferred following the procedure described in Section 2.3.2. After washing reaction residues and drying, the NiDI film was patterned by hand scratching to isolate a source/drain measurement area from a gate electrode. For protection of the source and drain electrode areas from the electrolyte during measurements, 10% CYTOP® solution was pasted and dried at 80°C for 10 min. $LiPF_6$ saturated bis(trifluoromethylsulfonyl)imide was prepared under an inert atmosphere, a small drop (~5 μg) of which was added onto the fabricated device to cover all the source, drain and gate electrodes.

2.4 Summary

NiDI was synthesized by the oxygen gas-promoted reaction, and its successful formation was confirmed by several spectroscopic, microscopic and theoretical techniques. In cyclic voltammetry measurements, NiDI was found to undergo two kinds of redox state transitions with Li^+/PF_6^- transport, which was also confirmed by IR and Raman spectroscopic measurements of the charged NiDI. Additionally, the charge transfer resistance of NiDI during the electrochemical reactions was found to be dependent on electrochemical potentials. The charge-discharge tests revealed that the specific capacity reached up to 155 mAh/g at 10 mA/g, with excellent cyclability confirmed by cycle tests at 250 mA/g. The mechanisms of the redox reactions of NiDI were studied by combination of experimental and theoretical methods, the results of which indicated the redox reactions mainly on the ligand. The electronic conductivity at different redox states were investigated using an organic electrochemical transistor with a NiDI film. At different electrochemical potentials, NiDI showed change of electronic conductivity; the NiDI film at the oxidized state showed higher conductivity.

As demonstrated with NiDI, a series of bis(diimino)metal coordination nanosheets is expected to be promising for energy storage applications. By taking advantage of structure tunability of those materials, further improvement of their properties would be enabled, aiming at superior energy storage functions.

2.5 Reference

1. (a) D. Herebian, E. Bothe, F. Neese, T. Weyhermüller, K. Wieghardt, *J. Am. Chem. Soc.* **2003**, *125*, 9116–9128.
   (b) A. L. Balch, R. H. HoIm, *J. Am. Chem. Soc.* **1966**, *88*, 5201–5209.
   (c) K. Chłopek, E. Bothe, F. Neese, T. Weyhermuller, K. Wieghardt, *Inorg. Chem.* **2006**, *45*, 6298–6307.
2. (a) D. Sheberla, L. Sun, M. A. Blood-Forsythe, S. Er, C. R. Wade, C. K. Brozek, A. Aspuru-Guzik, M. Dincă, *J. Am. Chem. Soc.* **2014**, *136*, 8859–8862.
   (b) D. Sheberla, J. C. Bachman, J. S. Elias, C. J. Sun, Y. Shao-Horn, M. Dincă, *Nat. Mater.* **2017**, *16*, 220–224.
3. (a) N. Lahiri, N. Lotfizadeh, R. Tsuchikawa, V. V. Deshpande, J. Louie, *J. Am. Chem. Soc.* **2017**, *139*, 19–22.
   (b) J. H. Dou, L. Sun, Y. Ge, W. Li, C. H. Hendon, J. Li, S. Gul, J. Yano, E. A. Stach, M. Dincă, *J. Am. Chem. Soc.* **2017**, *139*, 13608–13611.
   (c) D. Feng, T. Lei, M. R. Lukatskaya, J. Park, Z. Huang, M. Lee, L. Shaw, S. Chen, A. A. Yakovenko, A. Kulkarni, et al., *Nat. Energy* **2018**, *3*, 30–36.
   (d) E. J. H. Phua, K. H. Wu, K. Wada, T. Kusamoto, H. Maeda, J. Cao, R. Sakamoto, H. Masunaga, S. Sasaki, J. W. Mei, et al., *Chem. Lett.* **2018**, *47*, 126–129.
4. (a) B. T. O. Holt, M. A. Vance, L. M. Mirica, D. E. Heppner, T. D. P. Stack, E. I. Solomon, *J. Am. Chem. Soc.* **2009**, *131*, 6421–6438.
   (b) F. Hartl, D. J. Stufkens, A. Vlcek, *Inorg. Chem.* **1992**, *31*, 1687–1695.
   (c) Chongzhao Ran, C.; Xu, X.; Raymond, S. B.; Ferrara, B. J.; Neal, K.; Bacskai, B. J.; Medarova, Z.; Moore, A. *J. Am. Chem. Soc.*, **2009**, *131*, 15257–15261.
5. A. Mohtasebi, T. Chowdhury, L. H. H. Hsu, M. C. Biesinger, P. Kruse, *J. Phys. Chem. C* **2016**, *120*, 29248–29263.
6. (a) C. D. Batich, D. S. Donald, *J. Am. Chem. Soc.* **1984**, *106*, 2758–2761.
   (b) W. E. Swartz, R. A. Alfonso, *J. Electron Spectros. Relat. Phenomena* **1974**, *4*, 351–354.
7. S. O. Grim, W. E. Swartz, L. J. Matienzo, I. Yin, *Inorg. Chem.* **1973**, *12*, 2762–2769.
8. K. Sakaushi, G. Nickerl, F. M. Wisser, D. Nishio-Hamane, E. Hosono, H. Zhou, S. Kaskel, J. Eckert, *Angew. Chemie Int. Ed.* **2012**, *51*, 7850–7854.
9. (a) R. Aroca, M. Nazri, G. A. Nazri, A. J. Camargo, M. Trsic, *J. Solution Chem.* **2000**, *29*, 1047–1060.

(b) C. M. Burba, R. Frech, *J. Phys. Chem. B* **2005**, *109*, 15161–15164.

10. M. D. Levi, G. Salitra, B. Markovsky, H. Teller, D. Aurbach, U. Heider, L. Heider, *Society* **1999**, *146*, 1279–1289.
11. (a) X. Sun, K. H. Wu, R. Sakamoto, T. Kusamoto, H. Maeda, X. Ni, W. Jiang, F. Liu, S. Sasaki, H. Masunaga, et al., *Chem. Sci.* **2017**, *8*, 8078–8085.

    (b) T. Kambe, R. Sakamoto, T. Kusamoto, T. Pal, N. Fukui, K. Hoshiko, T. Shimojima, Z. Wang, T. Hirahara, K. Ishizaka, et al., *J. Am. Chem. Soc.* **2014**, *136*, 14357–14360.
12. P. Yu, N.N. Popov, J. A. Ritter, R. E. White, *J. Electrochem. Soc.* **1999**, *146*, 8-14.
13. (a) G. Férey, F. Millange, M. Morcrette, C. Serre, M. L. Doublet, J. M. Grenèche, J. M. Tarascon, *Angew. Chemie - Int. Ed.* **2007**, *46*, 3259–3263.

    (b) T. L. A. Nguyen, R. Demir-Cakan, T. Devic, M. Morcrette, T. Ahnfeldt, P. Auban-Senzier, N. Stock, A. M. Goncalves, Y. Filinchuk, J. M. Tarascon, et al., *Inorg. Chem.* **2010**, *49*, 7135–7143.

    (c) M. Okubo, D. Asakura, Y. Mizuno, J. D. Kim, T. Mizokawa, T. Kudo, I. Honma, *J. Phys. Chem. Lett.* **2010**, *1*, 2063–2071.

    (d) M. Nagarathinam, K. Saravanan, E. J. H. Phua, M. V. Reddy, B. V. R. Chowdari, J. J. Vittal, *Angew. Chemie - Int. Ed.* **2012**, *51*, 5866–5870.

    (e) D. Asakura, M. Okubo, Y. Mizuno, T. Kudo, H. Zhou, K. Ikedo, T. Mizokawa, A. Okazawa, N. Kojima, *J. Phys. Chem. C* **2012**, *116*, 8364–8369.
14. J. B. Goodenough, Y. Kim, *Chem. Mater.* **2010**, *22*, 587–603.
15. P. Giannozzi, S. Baroni, N. Bonini, M. Calandra, R. Car, C. Cavazzoni, D. Ceresoli, G. L. Chiarotti, M. Cococcioni, I. Dabo, et al., *J. Phys. Condens. Matter* **2009**, *21*, DOI 10.1088/0953-8984/21/39/395502.
16. (a) G. Greczynski, L. Hultman, *ChemPhysChem* **2017**, *18*, 1507–1512.

    (b) M. Yang, M. J. Marino, V. J. Bojan, O. L. Eryilmaz, A. Erdemir, S. H. Kim, *Appl. Surf. Sci.* **2011**, *257*, 7633–7638.

    (c) N. Schulz, R. Hausbrand, C. Wittich, L. Dimesso, W. Jaegermann, *J. Electrochem. Soc.* **2018**, *165*, A833–A846.
17. M. C. Militello, S. W. Gaarenstroom, *Surf. Sci. Spectra* **1999**, *6*, 141–145.
18. A. P. Grosvenor, M. C. Biesinger, R. S. C. Smart, N. S. McIntyre, *Surf. Sci.* **2006**, *600*, 1771–1779.
19. Gaussian 09, Revision E.01, Frisch, M. J.; Trucks, G. W.; Schlegel, H. B.; Scuseria, G. E.; Robb, M. A.; Cheeseman, J. R.; Scalmani, G.; Barone, V.; Mennucci, B.; Petersson, G. A.;

Nakatsuji, H.; Caricato, M.; Li, X.; Hratchian, H. P.; Izmaylov, A. F.; Bloino, J.; Zheng, G.; Sonnenberg, J. L.; Hada, M.; Ehara, M.; Toyota, K.; Fukuda, R.; Hasegawa, J.; Ishida, M.; Nakajima, T.; Honda, Y.; Kitao, O.; Nakai, H.; Vreven, T.; Montgomery, J. A., Jr.; Peralta, J. E.; Ogliaro, F.; Bearpark, M.; Heyd, J. J.; Brothers, E.; Kudin, K. N.; Staroverov, V. N.; Kobayashi, R.; Normand, J.; Raghavachari, K.; Rendell, A.; Burant, J. C.; Iyengar, S. S.; Tomasi, J.; Cossi, M.; Rega, N.; Millam, J. M.; Klene, M.; Knox, J. E.; Cross, J. B.; Bakken, V.; Adamo, C.; Jaramillo, J.; Gomperts, R.; Stratmann, R. E.; Yazyev, O.; Austin, A. J.; Cammi, R.; Pomelli, C.; Ochterski, J. W.; Martin, R. L.; Morokuma, K.; Zakrzewski, V. G.; Voth, G. A.; Salvador, P.; Dannenberg, J. J.; Dapprich, S.; Daniels, A. D.; Farkas, Ö.; Foresman, J. B.; Ortiz, J. V.; Cioslowski, J.; Fox, D. J. Gaussian, Inc., Wallingford CT, 2009.

20. (a) Z. G. Tao, X. Zhao, X. K. Jiang, Z. T. Li, *Tetrahedron Lett.* **2012**, *53*, 1840–1842.
(b) J. Mahmood, D. Kim, I. Y. Jeon, M. S. Lah, J. B. Baek, *Synlett* **2013**, *24*, 246–248.

Chapter 5

Concluding remarks

Throughout this thesis, I focused on bis(diimino)metal coordination nanosheets, aiming at electrochemical energy storage applications. The nanosheets consisting of different 3d transition metals were synthesized, and they were found to possess energy storage functions in lithium batteries, in which the electrochemical properties were tailored by the metal species.

In Chapter 1, I described the importance of MOFs and their applications, especially electrochemical energy storages. Electronically conductive coordination nanosheets, an emerging class of MOFs, are also introduced from the viewpoint of their exceptionally high conductivity.

In Chapter 2, I synthesized bis(diimino)nickel coordination nanosheet (NiDI), and its electrochemical properties including energy storage functions as an electrode in a lithium battery were studied. NiDI was found to show redox reactions based on multielectron transfer, which was accompanied with countercation/counteranion transport. This unique characteristic led to high specific capacity and good cyclability as a MOF-based cathode material. The mechanisms of these electrochemical behavior were investigated by both experimental and theoretical techniques, finding that the redox reactions occurred mainly on the ligands. Electronic conductivity of NiDI at different redox states were also examined, and it was revealed that conductivity of NiDI increased via an oxidation reaction, which reasonably explains the potential-dependent charge transfer resistance in the lithium battery.

In Chapter 3, I developed the coordination nanosheets with other 3d transition metals, CoDI and CuDI, and investigated effects of the metal species on electrochemical properties of the nanosheets. In electrochemical measurements, CoDI did not show obvious redox activity unlike NiDI although it possess the redox active ligand. This unexpected behavior was explained by kinetic factors such as sluggish ion transport. On the other hand, CuDI underwent redox reactions as observed with NiDI, and its specific capacity was far higher than NiDI and the other MOF-based cathode materials. The origin of the high capacity was revealed as valence state transitions of Cu(I)/Cu(II), which occurred on the antibonding orbitals of the Cu-N bond.

In Chapter 4, I synthesized the heterometal coordination nanosheet, $Co_xNi_{1-x}DI$, and investigated its electrochemistry-related properties. Characterization of the material revealed that the different metal species were randomly distributed in the framework to form a solid-solution state. This structure led to redox-activation of Co-centered motif by embedding a little amount of Ni atoms. As an energy storage material, $Co_xNi_{1-x}DI$ displayed higher specific

capacity than NiDI and CoDI in relatively negative voltage, which was possibly related to energy level differences of the antibonding orbitals around the metals and the heterometal crystal structures, being suggested by theoretical calculations and *ex situ* PXRD measurements.

To conclude my thesis, a series of bis(diimino)metal coordination nanosheets was synthesized. The electrochemical properties of these materials were found to be largely affected by the metal species, in which NiDI and CuDI showed noteworthy energy storage functions based on unique multielectron transfer reactions. Among numerous types of MOFs, this project shed light on the coordination nanosheets for energy storage applications, and successfully demonstrated the advantages of their unique redox properties and high electronic conductivity. Furthermore, the project gave us an insight into the energy storage functions on the redox-active anionic ligands, which will offer a guideline for development of novel energy storage systems based on cation-anion concerted redox activities.

Acknowledgement

I would like to show my gratitude to those who supported the accomplishment of my Ph.D. course research.

Professor Dr. Hiroshi Nishihara offered me generous support of helpful advice, the opportunity to carry out research. He has offered me environments to pursue my Ph.D. course study.

I would like to express appreciation to Associate Professor Dr. Yoshinori Yamanoi, Project Assistant Professor Dr. Mariko Miyachi, Project Assistant Professor Dr. Wu Kuo Hui, Project Assistant Professor Dr. Hiroaki Maeda and Project Assistant Professor Michihiro Nishikawa.

There are researchers supported my Ph.D. course study. I am thankful to Dr. Ken Sakaushi, Mr. Shin Kimura and Mr. Eiki Yasukawa (National Institute of Materials Science) for electrochemical measurements and related discussions. I would like to thank Dr. Keisuke Shinoda (National Institute of Materials Science) for transmission electron microscopy observation. I would give recognition to Professor Dr. Sono Sasaki (Kyoto Institute of Technology) for synchrotron radiation powder X-ray diffraction measurements and Professor Dr. Henning Sirringhaus (University of Cambridge) for organic electrochemical transistor measurements.

I am deeply grateful to all Nishihara Laboratory members. I give special thanks to my colleagues Mr. Ryojun Toyoda for encouraging me during my Ph.D. course. Finally, I would like to express my greatest appreciation to my family for mentally and financially supported me.

List of Publication

【Publications related to the thesis】

1. K. Wada, K. Sakaushi, S. Sasaki, H. Nishihara, *Angew. Chem. Int. Ed.* **2018**, *57*, 8886–8890.

【Publications not related to the thesis】

1. E. J. H. Phua, K.-H. Wu, K. Wada, T. Kusamoto, H. Maeda, J. Cao, R. Sakamoto, H. Masunaga, S. Sasaki, J.-W. Mei, W. Jiang, F. Liu, H. Nishihara, *Chem. Lett.* **2018**, *47*, 126-129.
2. R. Matsuoka, R. Toyoda, R. Shiotsuki, N. Fukui, K. Wada, H. Maeda, R. Sakamoto, S. Sasaki, H. Masunaga, K. Nagashio, H. Nishihara, *ACS Appl. Mater. Interfaces* **2019**, *11*, 2730-2733.
3. R. Sakamoto, R. Shiotsuki, K. Wada, N. Fukui, H. Maeda, J. Komeda, R. Sekine, K. Harano, H. Nishihara, *J. Mater. Chem. A* **2018**, *6*, 22189-22194.
4. T. Pal, S. Doi, H. Maeda, K. Wada, C. M. Tan, N. Fukui, R. Sakamoto, S. Tsuneyuki, S. Sasaki and H. Nishihara, *Chem. Sci.* **2019**, *10*, 5218-5225.